Designing Topological High-Order Van Hove Singularities: Twisted Bilayer Kagomé

David T. S. Perkins, Anirudh Chandrasekaran, and Joseph J. Betouras

Department of Physics, Loughborough University,
Loughborough LE11 3TU, England, United Kingdom

The interplay of high-order Van Hove singularities and topology plays a central role in determining the nature of the electronic correlations governing the phase of a system with unique signatures characterising their presence. Layered van der Waals heterostuctures are ideal systems for band engineering through the use of twisting and proximity effects. Here, we use symmetry to demonstrate how twisted Kagomé bilayers can host topological high-order Van Hove singularities. We study a commensurate system with a large twist angle and demonstrate how the initial choice of high-symmetry stacking order can greatly influence the electronic structure and topology of the system. We, furthermore, study the sublattice interference in the system. Our results illustrate the rich energy landscape of twisted Kagomé bilayers and unveil large Chern numbers (of order 10), establishing twisted bilayer Kagomé as a natural playground for probing the mixing of strong correlations and topology.

I. INTRODUCTION

Electronic instabilities are facilitated when the kinetic energy of electrons is dominated by the characteristic energy scale of their interactions, resulting in the emergence of different phases. Naturally, the study of vanishing Fermi velocities, occurrence of flat bands, and their associated divergences in the density of states (DOS) play a central role in determining the electronic phases, transport and thermodynamic properties of materials [1]. The simplest example of this is the Van Hove singularity (VHS), a saddle point within the band structure that yields a logarithmic divergence in the DOS [2]. More recently, higher-order VHSs (HOVHSs) and flat bands have attracted much attention due to their appearance in several systems exhibiting exotic behaviours such as $Sr_3Ru_2O_7$ [3–6], bernal bilayer graphene [7], twisted multilayer graphene and rhombohedral trilayer graphene [8–12], twisted bilayer WSe_2 [13], and supermetals [14] are a direct consequence of a HOVHS. The telltale sign of a HOVHS is a more severe divergence of the DOS, scaling according to a power-law rather than a logarithm [5, 15]. A detailed classification scheme for the various types of HOVHSs has been recently developed [15, 16] in conjunction with methods to engineer and analyse their nature [17] and robustness to disorder [18]. As a result, the exact connection between HOVHSs and the observed phenomena as well as methods to engineer quantum materials with desired properties as a consequence of HOVHSs and flat bands, are areas of intense research and discussion.

An exemplary system for probing the physics of strong correlations is the Kagomé lattice, which possesses a perfectly flat band across the entire Brillouin zone (BZ), whilst hosting Dirac electrons around the BZ corners and VHSs at the BZ edge. The Kagomé lattice with nearest-neighbour hopping is the line graph of a honeycomb lattice. Graph theory guarantees that such lattices possess at least one flat band [19–21]. At the same time, the Kagomé lattice appears in both its monolayer and bilayer forms in several materials including the vanadium-based antimonides (AV_3Sb_5; A = K, Rb, Cs) [22–25], $CsTi_3Bi_5$ [26, 27], and Kagomé magnets [28–30]. In these cases, the collection of atoms forming the Kagomé lattice are embedded in a network of atoms that do not form part of the Kagomé lattice. These atomic cages prevent band engineering through methods that have proven extremely powerful in the field of van der Waals (vdW) heterostructures, where various two-dimensional (2D) materials may be stacked and offset by a relative twist angle to manifest HOVHSs and flat bands, enable strong correlations, induce topological phases, and tune proximity-induced couplings [8, 10, 31–39]. There is a recent comprehensive study that predicts many more stoichiometric materials with Kagomé lattice structures [40]. An alternative family of 2D materials are metal-organic frameworks (MOFs), which may be constructed to host a Kagomé pattern without an atomic cage [41–47].

It is therefore natural to consider Kagomé-based vdW heterostructures when designing bespoke band structures exhibiting HOVHSs and near-flat bands which may be further tuned through straining [48] and twisting [49]. Moreover, topological Kagomé effects will become more accessible through the plethora of potential 2D partner materials and the tunability granted by twisting, allowing for the realisation of topological HOVHSs; these are expected to play a key role in the formation of phases when incorporating interactions. For example, the superconducting phase and charge ordering in AV_3Sb_5 are understood to stem from the topological nature of the band structure [50], suggesting that twisting may enrich the phase space of Kagomé materials. Topological VHSs have been studied in a 3D context via Weyl metals [51], whilst topological HOVHSs have only very recently been considered in a Kagomé monolayer [52].

In this work, we demonstrate how topological HOVHSs with two- (C_{2z}), three- (C_{3z}), and six-fold (C_{6z}) rotational symmetry can be engineered in twisted Kagomé bilayers for all possible high-symmetry stackings of the Kagomé bilayer [53], and how the choice of stacking can greatly influence the nature and number of HOVHSs present in the band structure. We introduce the

three high-symmetry stacking configurations and illustrate how the electronic structure is affected by tunneling asymmetry (dimerisation) and complex next-nearest-neighbour (NNN) hopping. We then show how the structural symmetry of the twisted bilayer Kagomé (TBK) is reduced upon twisting to a commensurate angle. Next, we model TBK using a tight-binding Hamiltonian including dimerisation, complex NNN tunneling, and an interlayer potential (i.e. out-of-plane electric field) to enable band engineering for creating topological HOVHSs. To establish HOVHSs and illustrate the importance of stacking order, we focus on TBK with a twist $38.2°$ corresponding to the minimum moiré unit cell achievable.

We find that monkey saddles (third-order VHSs) appear around the moiré BZ (MBZ) corners for a large range of parameter values in several bands, whilst cuspoid singularities (elongated VHSs) appear around the MBZ edges without any need for tuning, and identify two classes of singularities that arise for both. Moreover, the stacking configurations with an effective C_{6z} symmetry in momentum space also host very sensitive sixth-order HOVHSs at the centre of the MBZ. We use symmetry arguments to establish the exact number of singularities that may occur simultaneously within each band. Finally, when a HOVHS is created through the use of complex NNN tunneling, the breaking of time-reversal symmetry lifts the degeneracy between bands and allows us to calculate the Chern index for each one. We unveil bands with a Chern number of order 10 whilst simultaneously hosting a HOVHS, establishing a zoo of topological HOVHS in TBK. Given the growing family of Kagomé materials and the bespoke nature of vdW heterostructures, the results we present here will help the design of topological Kagomé HOVHSs and nearly flat bands with exciting properties.

II. HIGH-SYMMETRY STACKING AND COMMENSURATE TWISTING

A. Stacking Configurations

An untwisted bilayer formed of two identical Kagomé lattices has three high-symmetry stacking orders (Fig. 1a): AA, in which the sublattices of both layers are perfectly aligned and retains the D_{6h} symmetry of the monolayer; AB, where one layer is shifted by a bond length relative to the other, resulting in only two directly overlapping sublattices and reducing the point group symmetry to D_2; interlocked, reminiscent of Bernal stacked graphene, wherein the up triangles of one layer are aligned with the down triangles of the other layer to reduce the bilayer's symmetry to D_{3d}. The band crossing at the K point of the Brillouin zone is protected by inversion symmetry, C_i, and time-reversal symmetry, $\mathcal{T}$, meaning that only the AB bilayer will naturally have a gapped structure around the Dirac point of the original monolayer (Fig. 1b). We note that the band structure

around the K point for the AA and interlocked strongly resembles those of AA and Bernal stacked graphene, respectively. We interpret this as a triangle exchange symmetry, like that of the sublattice exchange symmetry in graphene [54], that can be either even (AA) or odd (interlocked). Details of each bilayer's Hamiltonian are provided in the Supplemental Material [55].

To achieve HOVHSs, it is necessary to eliminate the linear band crossings at the Dirac points in the twisted bilayer and gain control over the emergent gaps by breaking either C_i or $\mathcal{T}$; whether or not a Dirac cone can be flattened is ultimately determined by the symmetries of the system [56]. Inversion symmetry is broken in breathing Kagomé lattices whose up and down triangles are of different sizes, leading to an enhanced tunneling via up triangles and a reduced tunneling via down triangles (Fig. 1c) [57, 58]. Niobium halides [59], their chalcogen substituted counterparts [60], and Fe_3Sn_2 [28] are all examples of systems possessing such a lattice. To break $\mathcal{T}$, we may either apply a magnetic field or introduce a complex Haldane-type NNN tunneling [52, 61], whereby hopping anti-clockwise(clockwise) carries a phase factor of $e^{i\phi}$ ($e^{-i\phi}$) (Fig. 1d). Whilst both approaches will gap the Dirac cone, they ultimately yield different symmetries for the system. Dimerisation is a geometric effect and will reduce the point-group symmetry of the bilayer: $D_{6h} \to D_{3h}$, $D_{3d} \to C_{3v}$, and $D_2 \to D_1$. In contrast, Haldane-type hopping possesses a C_{6z} symmetry, thus not affecting the principal rotational symmetry. However, applying the in-plane dihedral rotation associated with the lattice will reverse the direction of the Haldane-type hopping ($e^{i\phi} \leftrightarrow e^{-i\phi}$). Therefore, the point-group symmetry will be reduced from $D_{6h} \to C_{6h}$, $D_{3d} \to C_{3v}$, and $D_2 \to C_{2z}$.

B. Commensurate Twist Angles

When introducing a twist into Kagomé bilayers, only certain angles will produce commensurate structures with a finite moiré unit cell (MUC), with smaller twists possessing larger MUCs and many thousands of lattice sites. Whether the bilayer is commensurate or not is determined by its underlying triangular lattice. We can label each twist angle yielding a commensurate bilayer, $\theta_c \in [0, 60°)$, by a unique pair of coprime integers, (m, n), such that [62–64]

$$\cos\theta_c = \frac{3m^2 - n^2}{3m^2 + n^2}, \quad \sin\theta_c = \frac{2\sqrt{3}\,mn}{3m^2 + n^2}, \qquad (1)$$

We apply the twist to the Kagomé bilayer by rotating one layer about a C_{6z} hexagon centre to maintain $60°$ twist periodicity, see Fig. 1a, and note that this labeling of commensurate angles yields two families [53, 64]: (i) where n is divisible by 3 and (ii) where n is not divisible by 3. These two sets can be simply related via $\theta'_c = \pi/3 - \theta_c$ such that if θ_c is defined by a choice of n that is divisible by 3, then θ'_c will be associated to a
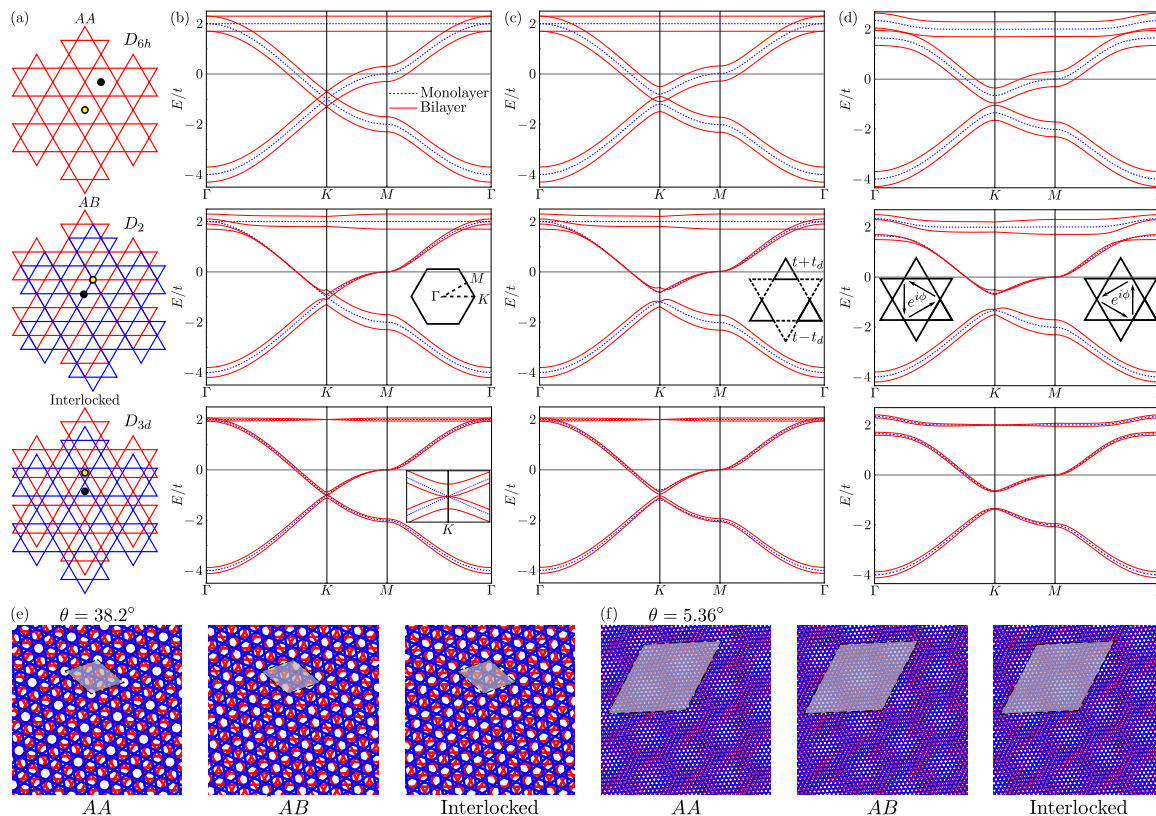
FIG. 1. Unique high-symmetry stacking orders of a Kagomé bilayer and their effect upon the band structure and moiré pattern. (a): High-symmetry stacking orders with their HSP highlighted by the yellow dot and twist centres used to create twisted bilayers denoted by the black dots. (b): Band structures associated to each stacking choice compared against the monolayer Kagomé bands in units of the intralayer tunneling amplitude, t. We use $t_\perp = 0.3t$ for the interlayer tunneling energy in the AA and AB stackings, whilst taking $\tilde{t}_\perp = 0.2t_\perp$ for the reduced interlayer hopping in the interlocked scenario due to no sites overlapping directly. The inset for the interlocked case shows how the Dirac cone is flattened. (c): Band structure under dimerisation ($t_d = 0.2t$) for the three stackings compared to the dimerised monolayer, with the bands being gapped out around the original MDP due to breaking of inversion symmetry. The schematic in the AB plot illustrates the enhancement/reduction (solid/dashed triangles) of tunneling energy due to dimerisation. (d): Band structure due to complex NNN tunneling with $t_H = 0.1t$ and $\phi = \pi/2$, with degeneracies being lifted by the breaking of $\mathcal{T}$. The schematics in the AB panel shows the hopping processes yielding phase factors of $e^{i\phi}$. Reversal of hopping direction instead yields $e^{-i\phi}$. (e)-(f): Moiré patterns for TBK with $(m,n) = (5,3)$ (e) and $(m,n) = (37,3)$ (f).

value of n that is not divisible by 3 [64]. For example, $(m,n) = (5,3)$ yields $\theta_c = 38.2°$ which in turn has the partner angle $\theta_c' = 21.8°$ which can be obtained with $(m,n) = (3,1)$. It was shown in Ref. [53] that the point group symmetries for both families of commensurate angles were identical when the twist is applied about a hexagon centre. However, differences between the two can be seen both at the superlattice level and in the Hamiltonian.

Working in the twist-symmetric frame (i.e. layer 1 is rotated by $-\theta_c/2$ and layer 2 is rotated by $\theta_c/2$), the cases where n is divisible by 3 will always possess a moiré lattice vector parallel to the x-axis, whilst those with n not divisible by 3 will always possess a moiré lattice vector parallel to the y-axis. Using graphene nomenclature, we refer to these orientations of the unit cell as zig-zag and armchair, respectively, based upon the Wigner-Seitz cell constructed with the twist origin at its centre. To see

this, let us denote the lattice sites of a triangular lattice by $\mathbf{r}_i(k,l) = k\mathbf{a}_1 + l\mathbf{a}_2$, where i is the layer index and $k,l \in \mathbb{Z}$, and their rotated forms by $\mathbf{r}_i^\theta = R_\theta \mathbf{r}_i$. In the twist-symmetric frame, the triangular lattice is guaranteed to have dihedral symmetry along the x-axis which manifests as a $y \to -y$ reflection symmetry between the layers. Consequently, a moiré lattice vector must lie either parallel to the x-axis or y-axis.

Without loss of generality [53], we assume that n is divisible by 3 such that $n = 3\nu$ with $\nu \in \mathbb{Z}$ and demand that the y-components of $\mathbf{r}_1^{\frac{\bar\theta_c}{2}}(k,l)$ and $\mathbf{r}_2^{\frac{\theta_c}{2}}(p,q)$ to vanish ($\bar\theta_c = -\theta_c$), we find that $\mathbf{r}_1^{\frac{\bar\theta_c}{2}}(k,l) = \mathbf{r}_2^{\frac{\theta_c}{2}}(p,q)$ is satisfied by

$$
\begin{aligned}
k &= \alpha_{m\nu}(m-\nu), & l &= 2\alpha_{m\nu}\nu, \\
p &= \alpha_{m\nu}(m+\nu), & q &= -2\alpha_{m\nu}\nu
\end{aligned}
\tag{2}
$$

where

$$\alpha_{m\nu} = \begin{cases} 1, & m+\nu \text{ is odd} \\ \frac{1}{2}, & m+\nu \text{ is even} \end{cases}. \quad (3)$$

The resulting moiré lattice constant is then $a_{\mathrm{M}} = \alpha_{m\nu}\sqrt{m^2 + 3\nu^2}$. If we instead demand that the y component vanish, we find a larger magnitude for the moiré lattice constant, $\tilde{a}_{\mathrm{M}} = \alpha_{m\nu}\sqrt{3}\sqrt{m^2 + 3\nu^2}$, clearly indicating that the commensurate superlattices defined by an n divisible by 3 will always be of zig-zag orientation. Alternatively, we may assume that $n = 3\nu \pm 1$ and demand that the x components of $\mathbf{r}_1^{\frac{\bar{\theta}_c}{2}}(k,l)$ and $\mathbf{r}_2^{\frac{\theta_c}{2}}(p,q)$ to vanish, where we find that $\mathbf{r}_1^{\frac{\bar{\theta}_c}{2}}(k,l) = \mathbf{r}_2^{\frac{\theta_c}{2}}(p,q)$ is satisfied when

$$\begin{aligned} k &= \alpha_{mn}(m+n), & l &= -2\alpha_{mn}m, \\ p &= \alpha_{mn}(m-n), & q &= -2\alpha_{mn}m, \end{aligned} \quad (4)$$

yielding a moiré lattice constant of $a_{\mathrm{M}} = \alpha_{mn}\sqrt{3m^2 + n^2}$. Similar to the $n = 3\nu$ case, we find a larger moiré lattice constant, $\tilde{a}_{\mathrm{M}} = \alpha_{mn}\sqrt{3}\sqrt{3m^2 + n^2}$, by seeking a moiré lattice vector parallel to the x-axis when n is not divisible by 3. Therefore, the orientation of the superlattice unit cell when 3 does not divide n will always be armchair. Lastly, we note that these two classes of superlattices are related by reflection in the $y = x$ line [55].

Moving onto the Hamiltonians of these systems, in the absence of complex NNN hopping and dimerisation, we see that the Hamiltonian with θ_c, $\mathcal{H}$, is related to the Hamiltonian with θ_c' by $\mathcal{H}(k_x, k_y) = \mathcal{H}'(k_y, k_x)$ when constructed in the twist-symmetric frame. Application of an out-of-plane electric field, which induces an interlayer potential, does not affect this observation. Including Haldane-type hopping, we must also flip the sign of the phase to obtain one Hamiltonian from the other, $\mathcal{H}(k_x, k_y, \phi) = \mathcal{H}'(k_y, k_x, -\phi)$. Finally, dimerisation results in the largest difference between the two systems, with the asymmetric tunnelling along up and down triangles appearing reversed in one layer and unchanged in the other after reflection in $y = x$. Specifically, the layer rotated clockwise by $\theta_c/2$ will appear to have its dimerisation unchanged whilst the layer rotated anti-clockwise by $\theta_c/2$ will have its dimerisation reversed, details are given in Ref. [55]. Therefore, the two families of twist angles may provide significant differences when dimerisation is present.

Finally, whilst the choice of stacking order might initially seem irrelevant for small twist angles, it becomes apparent at large twist angles that the superlattice structure is completely dependent on the stacking order (Fig. 1e,f). The point group symmetry of the resulting superlattice will always be dihedral and retain the rotational symmetry of the original untwisted Kagomé bilayer: D_6 for AA, D_3 for interlocked, and D_2 for AB [53]. This is further reflected in the electronic structure, where parabolic band touching at the K point is seen

for interlocked TBK whilst a double well with a linear crossing is seen for AA TBK.

III. MODEL

A. Tight-Binding Hamiltonian

We model the TBK system using a tight-binding model with one atomic orbital per lattice site, assuming an exponential decay of the tunneling energy with separation distance, r, of the form $f(r) = \exp(-\gamma(r - r_i)/r_i)$, where r_i is the nearest-neighbour separation ($\bar{a} = a/2$), for intralayer tunneling and the interlayer separation ($d_\perp$) for interlayer tunneling, whilst γ characterises the hopping range [49]. By retaining tunneling between all lattice sites up to NNN MUCs, the resulting momentum space Hamiltonian becomes:

$$\begin{aligned} H = &-\sum_{\mathbf{k}} \sum_l \sum_{\alpha,\beta} \left[t^{\alpha\beta}\Gamma_l^{\alpha\beta}(\mathbf{k}) - s_l\frac{\Delta}{2}\delta_{\alpha\beta} \right] c_{\mathbf{k}l\alpha}^\dagger c_{\mathbf{k}l\beta} \\ &-\sum_{\mathbf{k}} \sum_{\alpha,\beta} t_\perp^{\alpha\beta} \left[\Gamma_\perp^{\alpha\beta}(\mathbf{k}) c_{\mathbf{k}1\alpha}^\dagger c_{\mathbf{k}2\beta} + \text{h.c.} \right], \end{aligned} \quad (5)$$

where $c_{\mathbf{k}l\alpha}^\dagger$ ($c_{\mathbf{k}l\alpha}$) is the creation (annihilation) operator for an electron with momentum $\mathbf{k}$ in layer l for moiré sublattice site α, $t^{\alpha\beta} = t$ is the intralayer tunneling amplitude between sites α and β, $t_\perp^{\alpha\beta} = t_\perp$ is the interlayer tunneling amplitude between sites α and β of different layers, Δ is an interlayer potential, $s_l = \pm 1$ for layer 1/2, $\delta_{\alpha\beta}$ is the Kronecker delta, and $\Gamma_{l(\perp)}^{\alpha\beta}(\mathbf{k})$ are the structure factors containing the information about the decay of tunneling energy with distance (details in Ref. [55]). To include dimerisation, we restrict intralayer hopping to only nearest-neighbours and let $t^{\alpha\beta} = t \pm t_d$ with the sign determined by whether the tunneling is via an up or down triangle. For the models we consider here with $\gamma = 20$, nearest-neighbour intralayer tunnelling is sufficient to accurate model the system since NNN intralayer hopping introduces negligible corrections $\sim 10^{-7}t$. Alternatively, we may introduce an intralayer Haldane-type hopping via

$$H_{\mathrm{H}} = -t_{\mathrm{H}} \sum_{\mathbf{k}} \sum_l \sum_{\alpha,\beta} \Gamma_{\mathrm{H}}^{\alpha\beta}(\mathbf{k}) e^{i\mathcal{S}_{\alpha\beta}\phi} c_{\mathbf{k}l\alpha}^\dagger c_{\mathbf{k}l\beta}, \quad (6)$$

where $\mathcal{S}_{\alpha\beta} = \pm 1$ and the details of the Haldane structure factor, $\Gamma_{\mathrm{H}}^{\alpha\beta}(\mathbf{k})$, are given in Ref. [55]. Finally, we note that the Haldane hopping will not be subject to dimerisation due to being a NNN tunneling process. The total Hamiltonian is thus given by $\mathcal{H}(t_d, t_{\mathrm{H}}, \phi, \Delta; \theta) = H + H_{\mathrm{H}}$.

B. Electronic Structure and Stacking

We illustrate the effects of stacking order, dimerisation, and Haldane-type hopping in Fig. 2 for a TBK
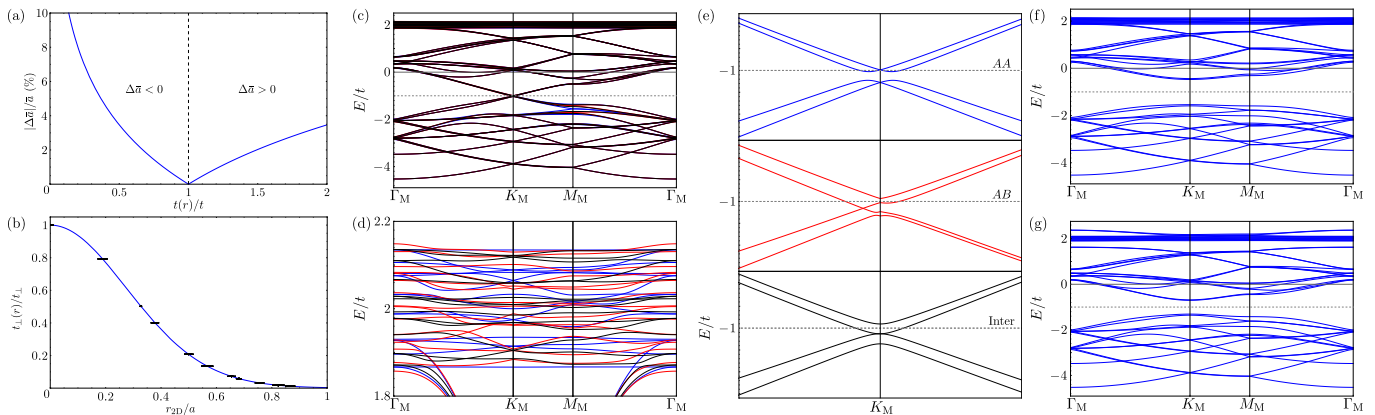
FIG. 2. Variation of the TBK band structure due to stacking, dimerisation, and Haldane-type hopping. Here we consider a TBK system with $\theta_c = 38.2°$, $a = 0.5338$ nm, $d_\perp = 0.6596$ nm, $t_\perp = 0.3t$, and $\gamma = 20$ [28, 49]. (a): Change in separation distance required to achieve a given decay factor for intralayer tunneling. (b): Effective error in interlayer atomic separations compared to the decay of interlayer tunneling energy for AA TBK. (c)-(e): Band structure in the absence of dimerisation and Haldane hopping for all high-symmetry stackings (blue: AA, red: AB, black: interlocked), with a focus on the near-flat band region (d) and on the MDP energy (e) marked by the grey dashed line. (f): The effect of dimersiation on AA TBK with $t_d = 0.2t$, opening a gap between bands 14 and 15. Similar band structures for AB and interlocked TBK are obtained, with differences in stacking order becoming more apparent over a wider range of the high-symmetry path, see Ref. [55]. (g): AA TBK with $t_H = 0.1t$ which opens two gaps: one between bands 14 and 15, and a second between bands 28 and 29.

system based on Fe_3Sn_2 [28, 49]. For a physical interpretation of dimerisation in TBK systems, we note that dimerisations as large as $t_d \sim 0.5t$ are achievable with small changes to the interatomic distances on the order of a 2-3% (Fig. 2a). Therefore, the dimerisation term approximates well a TBK system comprised of breathing Kagomé lattices at large twist angles. The effective separation error compared to the modelled interlayer tunneling decay is presented in Fig. 2b. Small changes to the tunneling energies will only renormalise the values of the parameters needed to tune a HOVHS.

Starting from $t_d = t_H = 0$, we see that the stacking order is particularly relevant around the M_M point with clear differences in both energy and structure (Fig. 2c). We further observe the appearance of a characteristic densely packed near-flat band region about the original monolayer flat band energy with a resolution of $\sim 0.3t$, where the stacking order greatly influences the fine details of each band, although no choice of stacking order prevents the loss of an exact flat band (Fig. 2d). The nature of the electronic structure of the aligned bilayer at the K_M point is also preserved upon twisting to a commensurate angle (Fig. 2e). Specifically, the gap and linear band crossing of the AA system persists whilst the interlocked stacking retains its parabolic band touching at the K_M point, with both sets of features occurring close to the original monolayer Dirac point (MDP) energy. These features prevent us from observing critical points that also possess a vanishing curvature in the absence of dimerisation or Haldane-type hopping.

C. Emergent Symmetries that enable HOVHSs

Through dimerisation and Haldane-type hopping, we can tune the gaps between previously degenerate bands at the K_M point to engineer a monkey saddle singularity for both the AA and interlocked TBK systems (Figs. 2f,g). This type of HOVHS requires C_{3z} symmetry and therefore cannot be hosted by the AB configuration. Moreover, we can explore the possibility of engineering a HOVHS with six-fold rotational symmetry at Γ_M in both the AA and interlocked TBK systems. Naturally, this will be achieved most easily using an AA stacking due to its inherent C_{6z} symmetry. When $t_d \neq 0$ and $t_H = 0$ the system possesses an effective C_{6z} symmetry in momentum space due to the system possessing C_{3z} and $\mathcal{T}$ (the same is true for interlocked TBK). For the opposite case with $t_d = 0$ and $t_H \neq 0$, the Haldane hopping leaves the structural C_{6z} symmetry intact. If both $t_d, t_H \neq 0$, then an effective C_{6z} symmetry cannot emerge either in AA or interlocked TBK through the combination of C_{3z} and $\mathcal{T}$. This does not prevent us from creating a six-fold singularity, due to deeper underlying symmetries present in the system.

Both AA and interlocked TBK possess a C_{3z} point group symmetry when dimerisation and complex NNN tunneling are included. By working in the twist-symmetric frame, the underlying moiré superlattice (i.e. neglecting dimerisation and Haldane-type hopping) will always exhibit a dihedral symmetry along the x-axis, y-axis, or sometimes both. For AA TBK the underlying superlattice possesses dihedral symmetry along both axes for all commensurate twist angles: $\mathcal{D}_x$ along the x-axis and $\mathcal{D}_y$ along the y-axis. In contrast, the underly-

TABLE I. A summary of the maximum number of HOVHSs allowed around the high-symmetry points of the MBZ for AA and interlocked TBK. The entries in the left section of the table indicate which tuning parameters are present, whilst the middle section lists the symmetries that are preserved. The right section of the table lists the number of second-, third- and sixth-order singularities permitted to occur simultaneously for that combination of symmetries for the two stacking orders. The subscripts denote the MUC orientation and stacking order where their number of singularities differ.

t_d	t_H	Δ	Zig-zag/Armchair AA	Zig-zag Interlocked	Armchair Interlocked	HOVHSs (2nd, 3rd, 6th)
✗	✗	✗	$C_{6z}, \mathcal{T}, \mathcal{D}_x, \mathcal{D}_y, \mathcal{D}_x\mathcal{T}, \mathcal{D}_y\mathcal{T}$	$C_{3z}, \mathcal{T}, \mathcal{D}_x, \mathcal{D}_x\mathcal{T}$	$C_{3z}, \mathcal{T}, \mathcal{D}_y, \mathcal{D}_y\mathcal{T}$	$(3,2,1)$
✓	✗	✗	$C_{3z}, \mathcal{T}, \mathcal{D}_y, \mathcal{D}_y\mathcal{T}$	$C_{3z}, \mathcal{T}$	$C_{3z}, \mathcal{T}, \mathcal{D}_y, \mathcal{D}_y\mathcal{T}$	$(3,2,1)$
✗	✓	✗	$C_{6z}, \mathcal{D}_x\mathcal{T}, \mathcal{D}_y\mathcal{T}$	$C_{3z}, \mathcal{D}_x\mathcal{T}$	$C_{3z}, \mathcal{D}_y\mathcal{T}$	$(3,2,1)$
✓	✓	✗	$C_{3z}, \mathcal{D}_y\mathcal{T}$	C_{3z}	$C_{3z}, \mathcal{D}_y\mathcal{T}$	$(3,2,1)_{○}, (3,1,0)_{◐}$
✗	✗	✓	$C_{6z}, \mathcal{T}$	$C_{3z}, \mathcal{T}$	$C_{3z}, \mathcal{T}$	$(3,2,1)$
✓	✗	✓	$C_{3z}, \mathcal{T}$	$C_{3z}, \mathcal{T}$	$C_{3z}, \mathcal{T}$	$(3,2,1)$
✗	✓	✓	C_{6z}	C_{3z}	C_{3z}	$(3,2,1)_{AA}, (3,1,0)_{\mathrm{Int}}$
✓	✓	✓	C_{3z}	C_{3z}	C_{3z}	$(3,1,0)$

ing superlattice of interlocked TBK will possess only $\mathcal{D}_x$ ($\mathcal{D}_y$) for a zig-zag (armchair) orientation. These symmetries produce the following mappings $\mathcal{D}_x : (y, z; \phi) \rightarrow (-y, -z; -\phi)$ and $\mathcal{D}_y : (x, z; -\phi) \rightarrow (-x, -z; -\phi)$, which may be interpreted as $(k_y, \phi) \rightarrow (-k_y, -\phi)$ and $(k_x, \phi) \rightarrow (-k_x, -\phi)$, respectively, and an exchange of layers. Dimerisation acts as a $\mathcal{D}_x$ breaking mechanism, due to mapping of up triangles to down triangles upon a layer exchange. The topologically trivial part of the Hamiltonian with $\Delta = 0$, H_0, is therefore symmetric under time-reversal in all cases and $\mathcal{D}_y$ for AA and armchair interlocked TBK when dimerisation is present,

$$H_0 = \mathcal{T} H_0 \mathcal{T}^{-1}, \quad H_0^{\mathrm{AA}} = \mathcal{D}_y H_0^{\mathrm{AA}} \mathcal{D}_y^{-1}$$
$$H_0^{\mathrm{Int},○} = \mathcal{D}_y H_0^{\mathrm{Int},○} \mathcal{D}_y^{-1}, \quad (7)$$

where the superscript denotes the stacking configuration and MUC orientation (○: armchair, ◐: zig-zag). If dimerisation is absent, $H_0 \rightarrow \bar{H}_0$, then up and down triangles are equivalent, and hence the topologically trivial piece of the Hamiltonian for zig-zag interlocked TBK retains its dihedral symmetry,

$$\bar{H}_0^{\mathrm{AA}} = \mathcal{D}_x \bar{H}_0^{\mathrm{AA}} \mathcal{D}_x^{-1} \qquad \bar{H}_0^{\mathrm{Int},○} = \mathcal{D}_x \bar{H}_0^{\mathrm{Int},○} \mathcal{D}_x^{-1}. \quad (8)$$

The topological contribution to the Hamiltonian is not symmetric under any diherdral rotation nor time-reversal,

$$\mathcal{T} H_\mathrm{H} \mathcal{T}^{-1} = H_\mathrm{H}|_{\phi \rightarrow -\phi}, \quad \mathcal{D} H_\mathrm{H} \mathcal{D}^{-1} = H_\mathrm{H}|_{\phi \rightarrow -\phi}, \quad (9)$$

but it is symmetric under their combined transformation,

$$H_\mathrm{H} = \mathcal{D}\mathcal{T} H_\mathrm{H} (\mathcal{D}\mathcal{T})^{-1}. \quad (10)$$

This results in the total Hamiltonian exhibiting emergent dihedral time-reversal symmetries for AA TBK and interlocked TBK (eqs. 7, 8, and 10), $\mathcal{H}_0 = \mathcal{D}\mathcal{T} \mathcal{H}_0 (\mathcal{D}\mathcal{T})^{-1}$.

The combinations of $\mathcal{D}_x\mathcal{T}$ and $\mathcal{D}_y\mathcal{T}$ manifest as $k_y \rightarrow -k_y$ and $k_x \rightarrow -k_x$ symmetries, respectively, in the 2D MBZ. By expanding the energy of a given band about the origin, the $\mathcal{D}\mathcal{T}$ and C_{3z} symmetries of the Hamiltonian restrict the expansion to

$$E \simeq \tilde{a}_2 k^2 + \tilde{a}_4 k^4 + \tilde{a}_6 k^6 + a_3 k^3 \cos(3\varphi)$$
$$+ b_3 k^3 \sin(3\varphi) + a_6 k^6 \cos(6\varphi) + \mathcal{O}(k^8), \quad (11)$$

where φ is the azimuthal angle and $\tilde{a}_n$, a_n, and b_n are coefficients that are functions of the tuning parameters. Therefore, symmetry allows for the emergence of a six-fold HOVHS provided that $\mathcal{D}\mathcal{T}$ (an effective reflection symmetry in either the x- or y-axis) and C_{3z} symmetry is preserved.

Taking this symmetry analysis one step further, we determine how many singularities exist at the same energy. In the twist-symmetric frame, we note that the zig-zag and armchair orientations of the MUC may yield different numbers of HOVHSs possessing the same energy due to the difference in their dihedral symmetries. Let us start by assuming that a monkey saddle exists at the K_M point of the MBZ. If $\mathcal{T}$ is preserved, K_M trivially maps onto K'_M, thereby yielding two simultaneous singularities. Introducing Haldane-type hopping breaks $\mathcal{T}$ and $\mathcal{D}$ symmetries, but leaves the $\mathcal{D}\mathcal{T}$ symmetries in tact, allowing us to again connect the differing MBZ corners for zig-zag (armchair) AA and interlocked TBK using $\mathcal{D}_x\mathcal{T}$ ($\mathcal{D}_y\mathcal{T}$). Only with both Haldane-type hopping and dimerisation do the two orientations differ for both stacking orders, wherein $\mathcal{D}_x\mathcal{T}$ is broken in zig-zag structures and $\mathcal{D}_y\mathcal{T}$ is preserved in armchair structures. Hence with both dimerisation and complex NNN hopping, zig-zag TBK will possess only a single HOVHS at a given MBZ corner energy, whilst armchair TBK will still exhibit two simultaneous singularities. Moving on to the case of second-order VHSs at the MBZ edges, the number of simultaneous singularities will always be three in AA and interlocked TBK due to possessing a C_{3z} symmetry. Only in AB TBK will the number of simultaneous singularities differ to become two instead of three due to its lack of C_{3z} symmetry. When dimerisation is introduced, AB TBK will always exhibit a dihedral symmetry along one of three lines: the y-axis (i.e. the $90°$ line) or the $\pm30°$ lines. These will always act to map two differing MBZ edges onto one another whilst leaving one to map onto iteslf. We summarise the maximum number of singularities occurring simultaneously for each possible combination of tuning parameters in Table I for AA and interlocked TBK.
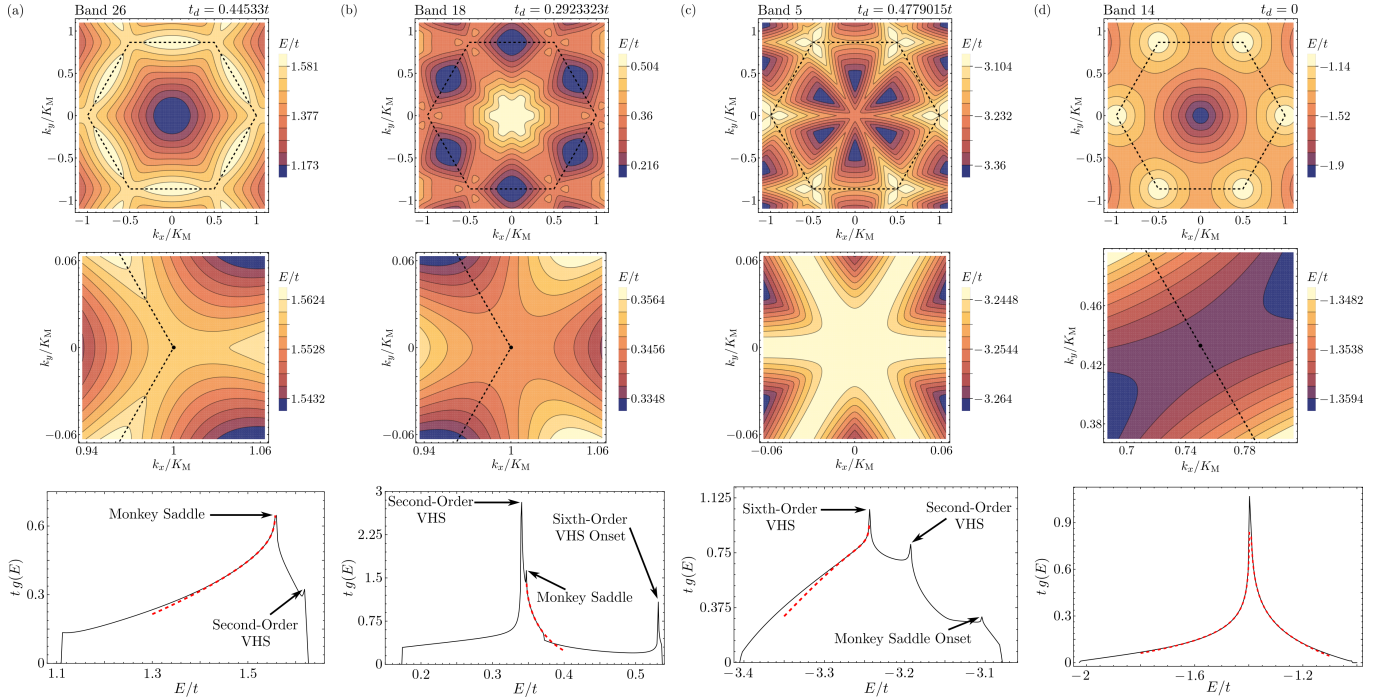
FIG. 3. Here we present the contours of bands hosting HOVHSs at K_M in (a) and (b), Γ_M in (c), and M_M in (d) due to dimerisation. The momentum is scaled to the K_M point and the black dashed line indicating the boundary of the first MBZ. The top row shows the energy surfaces over the entire MBZ, whilst the second row focuses on the relevant HOVHS. The bottom row shows the corresponding single-spin DOS per unit volume for the band. The red dashed lines are fittings of the expected HOVHS behaviour in the vicinity of the divergence (more details are provided in Ref. [55]). The AA TBK system considered here takes $\theta_c = 38.2°$, $a = 0.5338$ nm, $d_\perp = 0.6596$ nm, $t_H = 0$, $t_\perp = 0.3t$, and $\gamma = 20$ [28, 49]. The band number and choice of t_d are given at the top of each column.

IV. CREATING HIGHER-ORDER VAN HOVE SINGULARITIES

A. Monkey Saddle Singularities

Using a large range of dimerisations, $0.05 \lesssim t_d/t \lesssim 0.7$, the linear band crossings at the MBZ corners are gapped out to create monkey saddles. This results in two types of singularities. Band 26 of dimerised AA TBK in Fig. 3a illustrates a *delocalised* monkey saddle characterised by energy contours connecting the singularities at K_M and K'_M. In contrast, band 18 (Fig. 3b) hosts *localised* HOVHS at the MBZ corners which are disconnected from one another. Both cases yield a divergence in the DOS that is well described by a $g(\varepsilon) \sim \varepsilon^{-1/3}$ power-law at leading order (bottom panels of Figs. 3a,b), where ε is the energy measured from the singularity. The fits shown here account for sub-leading order corrections due to the HOVHS existing within a more complex energy landscape. The details and further examples of monkey saddles in other bands for AA and interlocked TBK can be found in Ref. [55].

Both of these types of singularities are of particular relevance to metals exhibiting non-Fermi liquid behaviour in their transport coefficients and thermodynamic properties. The presence of remote regions where the Fermi velocity vanishes (i.e. localised singularities) has been shown to alter the electrical resistivity of materials by acting as reservoirs for the current carrying electrons to scatter to and from [6] and heat capacity [5]. Similarly, the appearance of singularities on a single Fermi surface that has both dispersive and flat regions (i.e. delocalised singularities) have been shown to dominate the interaction-induced electron self-energy, thereby governing the electronic contribution to thermal transport [65].

B. Six-Fold Singularities

Due to its high-order nature, a six-fold singularity is very sensitive to the tuning parameters and may require several to achieve an exact HOVHS. However, symmetry can reduce the number of tuning parameters necessary to yield an effective sixth-order singularity from the perspective of experiment. Fig. 3c presents an example of a six-fold singularity achieved using only dimerisation. Our analysis of the expansion coefficients in eq. 11 reveals that band 5 has a vanishing second-order coefficient ($\tilde{c}_2 = 0$) and a fourth-order coefficient we infer to be small in comparison to the sixth-order term, $\tilde{c}_4 \ll c_6$: we obtain $\tilde{c}_4$ to be non-zero but observe an extremely small minimum in the band $(E(\mathbf{0}) - E(0.01\mathbf{K}_M))/E(\mathbf{0}) \sim 10^{-7}$.
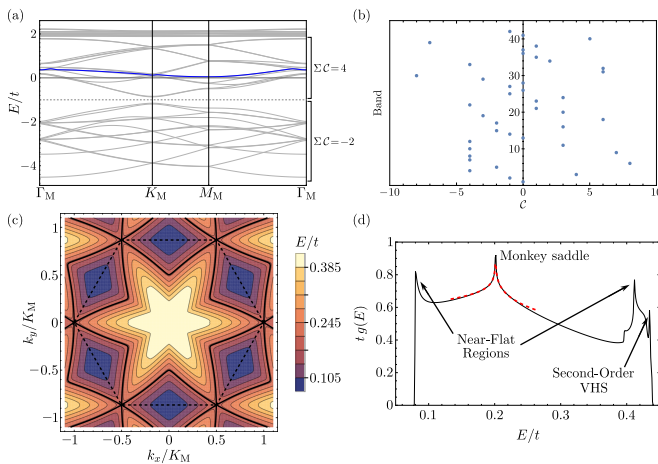
FIG. 4. Here we consider AA TBK tuned to host a topological monkey saddle with $\theta_c = 38.2°$, $a = 0.5338$ nm, $d_\perp = 0.6596$ nm, $t_H = 0.18147t$, $\phi = \pi/2$, $t_\perp = 0.3t$, and $\gamma = 20$ [28, 49]. (a): Band structure with the monkey saddle host band highlighted (band 20). The sum of the Chern numbers for the first and second sets of 14 bands are indicated. (b): The set of Chern numbers for each band. (c): Energy contours of band 20 across the entire MBZ whose boundary is marked by the dashed line and HOVHS energy contour is highlighted by the bold line. (d): Single-spin DOS per unit volume for band 20 hosting a topological monkey saddle. The red dashed line marks our fitting of the monkey saddle divergence whose leading order behaviour is $g(\varepsilon) \propto \varepsilon^{-1/3}$.

Moreover, the divergence of the DOS at the HOVHS energy is easily fitted by the $g(\varepsilon) \sim \varepsilon^{-2/3}$ scaling at leading order characteristic of a sixth-order singularity [15, 66], see Fig. 3c. The onset of a six-fold singularity can also be seen in other bands. The third peak in the DOS of band 18 (Fig. 3b) can be attributed to a set of six closely packed second-order singularities: closer inspection reveals a small minimum at the origin. We provide additional examples of effective six-fold HOVHSs in Ref. [55] for AA and interlocked TBK, with the latter being tuned via an interlayer potential.

C. Second-Order Singularities

The appearance of singularities (either localised or delocalised) with a two-fold symmetry at the M_M is expected in TBK given the VHSs that exist at the BZ edges of the monolayer. We immediately note that no tuning is required to observe singularities at the MBZ edges as demonstrated by band 14 in Fig. 3d. The HOVHS shown here takes the form $E \sim k_x^2 - k_y^4$ to produce a $g(\varepsilon) \sim D_\pm|\varepsilon|^{-1/4}$ scaling, where D_+ (D_-) is the prefactor for $\varepsilon > 0$ ($\varepsilon < 0$) whose ratio we find to match the expected value of $D_-/D_+ = \sqrt{2}$ [15]. We note that even with dimerisation included, these two-fold singularities can persist as in band 26 which hosts extremely flat singularities at its MBZ edges, yielding the second peak in

the DOS plot of Fig. 3a. Second-order singularities may also form away from the MBZ edges along Γ_M-K_M high-symmetry line, as seen in Figs. 3b,c for bands 18 (first DOS peak) and band 5 (second DOS peak). Finally, we observe that it may also be possible to engineer fourth-order singularties around the MBZ edges. We show in Ref. [55] that band 4 hosts two second-order singularities close to the M_M point, which may be tunable via parameters beyond those considered here.

D. Topological Monkey Saddles

Complex NNN hopping is an alternative way to gap out the Dirac cones that appear at MBZ corners, creating monkey saddle singularities through the breaking of $\mathcal{T}$. We show in Fig. 4 the electronic structure for a AA TBK with a purely imaginary NNN hopping tuned to yield a delocalised monkey saddle in band 20. We find that all degeneracies are lifted to result in the majority of bands becoming topologically non-trivial, with Chern numbers as large as $|\mathcal{C}| = 8$ being observed in bands 6 and 30 (Fig. 4b). Two major gaps open in the band structure and split the bands into three equal sets of 14 bands, with the lowest energy set giving a total Chern number of -2 whilst the middle energy set possesses a total Chern number of 4. Therefore, the AA TBK system will also become a Chern insulator exhibiting topologically protected edge states yielding an intrinsic anomalous Hall conductivity of $\sigma_{yx}^{int} = \pm 2e^2/h$ in these gaps.

Regarding band 20, it acts as a host of a delocalised topological HOVHS with a Chern number of $\mathcal{C} = 3$. The DOS for this band (Fig. 4d) reveals multiple singularities: a set of six closely situated second-order VHSs near the origin approaching a sixth-order singularity near the top of the band, and two regions where the band becomes extremely flat. The monkey saddle peak is well fitted by a DOS with a leading order correction that scales as $g(\varepsilon) \propto \varepsilon^{-1/3}$. We provide further examples of topological monkey saddles in Ref. [55]. Changing the stacking from AA to interlocked, another delocalised topological monkey saddle is revealed (at $t_H = 0.26589t$ and $\phi = \pi/2$) with a Chern number $\mathcal{C} = 9$.

E. The Role of Sublattice Interference

Nesting vectors act to enhance particle-hole fluctuations by connecting large parallel sections of the Fermi surface and can play a crucial role in the formation of different phases [67]. However, sublattice interference in a monolayer Kagomé can greatly effect these vectors by requiring that they further connect sections of the Fermi surface with the same sublattice projection [68]. Specifically, it has been shown that the critical contour associated to the VHS at 5/12 filling has six nesting vectors, as opposed to the three we might expect akin to graphene tuned to its VHS, which connect the BZ corners to the
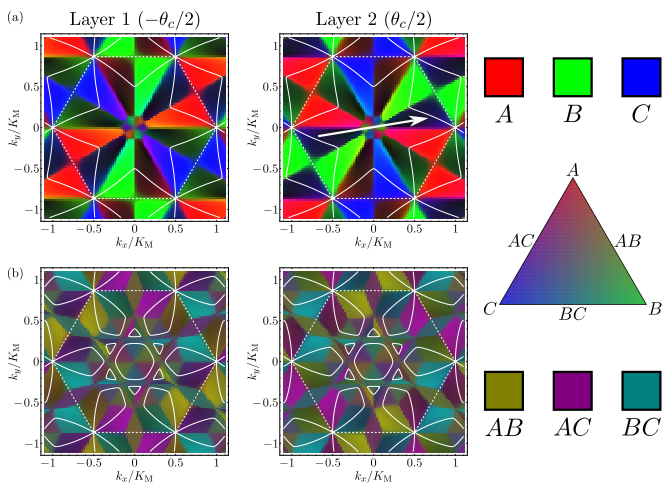
FIG. 5. Colour maps for two bands in AA TBK tuned to host a monkey saddle singularities at the MBZ corners indicating their sublattice projection throughout the MBZ within the bottom (left) and top (right) layers. If the eigenstate is completely localised to a sinlge sublattice it is given a colour of red (A), green (B), or blue (C). However, if the state is equally localised between two sublattices, it is given by equal mixing of their respective colours. The white contours highlight the Fermi surface at the critical energy of the HOVHS and the white dashed hexagon indicates the MBZ boundary. The white arrow is an example of a possible nesting vector between Fermi surface regions related by a π rotation. In both cases we use $\theta_c = 38.2°$, $a = 0.5338$ nm, $d_\perp = 0.6596$ nm, $t_\perp = 0.3t$, and $\gamma = 20$ [28, 49]. (a): Band 20 with $t_H = 0.18147t$ and $\phi = \pi/2$. (b): Band 8 with $t_d = 0.0862t$.

opposing edge M points [68]. This results in a preference for f-wave superconductivity in a Kagomé Hubbard system. However, for AA TBK, whilst the energy contours associated to the various HOVHSs are not simple hexagons, we may still identify nesting vectors that connect alternative sections of the Fermi surface that are related to one another by a π rotation about the z-axis, see Fig. 5a. The precise nesting vectors depend on the filling and the associated shape of the Fermi surface, but from the symmetry point of view, it is possible for them to survive. The symmetries of the Fermi surface respect at least those of the BZ as refined here.

By projecting the eigenstates for TBK onto the A, B, and C sublattices of the first and second layers, we observe a similar sublattice polarisation pattern across the entire MBZ that matches with that seen for monolayer Kagomé in Ref. [68]. Specifically, the Fermi surface sections that possess the same sublattice polarisation form a C_{2z} symmetry, see Fig. 5, thus matching the natural nesting vectors that can be inferred directly from the Fermi surface contour. This would suggest that sublattice interference specifically is unlikely to have as large an effect as in the monolayer for these cases. However, other singularities exist within the TBK band structure with vastly different Fermi surface shapes, meaning we cannot rule out sublattice interference as a means to re-

strict the nesting vectors beyond the requirements of the Fermi surface geometry. The sublattice projections of the bands reveal that the eigenstates can either be localised primarily on a single sublattice or between two sublattices. Band 20 in Fig. 5a shows the former case whilst band 8 in Fig. 5b exhibit the latter with admixing between sublattices. Finally, we note that the dihedral symmetry along the x-axis is clearly illustrated by the sublattice projections of the two layers in Fig. 5, with A and A' mapping onto one another, whilst B (C) maps onto C' (B') for the $\theta_c = 38.2°$ AA TBK system [55].

V. DISCUSSION

In this article, we have presented a detailed analysis of the symmetries and band structure for twisted bilayer Kagomé vdW heterostuctures for a large commensurate twist angle and identified its potential to host exotic topological HOVHS. Specifically, we encountered three types of Van Hove singularity in the band structure: monkey saddles around the K_M point, six-fold singularities around Γ_M, and two-fold singularities at the M_M point. These singularities could be achieved through the use of dimerisation, an applied out-of-plane electric field, and complex NNN hopping. The monkey saddle singularities were found to occur in several bands and for a large range of tuning parameters, making them relatively accessible as they can be expected to occur in a plethora of TBK systems. In studying this type of singularity, we classified them into two categories: delocalized and localized. Both types of singularity can be expected to have significant effects on the electric and thermal transport coefficients, shifting them from the typical Fermi liquid behaviour. Through complex hopping, we also found them to emerge in topological bands, creating topological HOVHSs. This suggests that TBK hosts a rich landscape of transport phenomena ranging from non-Fermi liquid behaviour to topologically protected edge states.

Symmetry analysis identified the combination of dihedral rotation and time reversal, $\mathcal{DT}$, to play a central role in determining the number of possible HOVHS that may occur simultaneously. The application of an out-of-plane electric field acts to break this symmetry and reduce the number of HOVHSs. We expect that the AA and interlocked stackings will have similar properties and phase diagrams when they possess the same symmetries. This is not the case when Haldane tunneling is included whilst dimerisation is absent. In contrast, the AB system is likely to exhibit the most unique phase diagram because it only hosts singularities with C_2 symmetry. If we consider a scenario where AB TBK is in the same phase as the AA and interlocked systems, then we would still expect unique signatures in the transport coefficients and electron self-energy courtesy of the different types of HOVHS [6, 65]. The results presented here act as a guide to how topological HOVHSs can be achieved when constructing vdW heterostructures with Kagomé patterns.

Currently, there are several candidate systems in which to probe these ideas: the largest class of candidate materials are MOFs, but recently N-doped Kagomé graphene and 2D π-conjugated polymers have been synthesised, realising Kagomé patterns formed predominantly of triangular carbon atom islands [69, 70]. There is intensive research for more materials of Kagomé structure where the results of this work are relevant. Regarding other lattices, the same symmetries occur in hexagonal or triangular lattices. The dense flat band region of the bilayer Kagomé though, which led to the rich structure of HOVHSs is the reason that we took this lattice as an example. Future work will focus on the role of interactions in the TBK system to discover how the flat bands and the plethora of topological HOVHSs influence phase formation.

[1] L. Classen and J. J. Betouras, High-Order Van Hove Singularities and Their Connection to Flat Bands, Annu. Rev. Condens. Matter Phys. 10.1146/annurev-conmatphys-042924-015000 (2024).

[2] L. Van Hove, The Occurrence of Singularities in the Elastic Frequency Distribution of a Crystal, Phys. Rev. 89, 1189 (1953).

[3] S. A. Grigera, R. S. Perry, A. J. Schofield, M. Chiao, S. R. Julian, G. G. Lonzarich, S. I. Ikeda, Y. Maeno, A. J. Millis, and A. P. Mackenzie, Magnetic Field-Tuned Quantum Criticality in the Metallic Ruthenate $Sr_3Ru_2O_7$, Science 294, 329 (2001).

[4] A. Tamai, M. P. Allan, J. F. Mercure, W. Meevasana, R. Dunkel, D. H. Lu, R. S. Perry, A. P. Mackenzie, D. J. Singh, Z.-X. Shen, and F. Baumberger, Fermi Surface and van Hove Singularities in the Itinerant Metamagnet $Sr_3Ru_2O_7$, Phys. Rev. Lett. 101, 026407 (2008).

[5] D. V. Efremov, A. Shtyk, A. W. Rost, C. Chamon, A. P. Mackenzie, and J. J. Betouras, Multicritical fermi surface topological transitions, Phys. Rev. Lett. 123, 207202 (2019).

[6] C. H. Mousatov, E. Berg, and S. A. Hartnoll, Theory of the strange metal $Sr_3Ru_2O_7$, Proceedings of the National Academy of Sciences 117, 2852 (2020).

[7] Y.-C. Lee, D. V. Chichinadze, and A. V. Chubukov, Crossover from ordinary to higher order Van Hove singularity in a honeycomb system: A parquet renormalization group analysis, Phys. Rev. B 109, 155118 (2024).

[8] Y. Cao, V. Fatemi, S. Fang, K. Watanabe, T. Taniguchi, E. Kaxiras, and P. Jarillo-Herrero, Unconventional superconductivity in magic-angle graphene superlattices, Nature 556, 43 (2018).

[9] H. Zhou, T. Xie, T. Taniguchi, K. Watanabe, and A. F. Young, Superconductivity in rhombohedral trilayer graphene, Nature 598, 434 (2021).

[10] J. M. Park, Y. Cao, L.-Q. Xia, S. Sun, K. Watanabe, T. T., and P. Jarillo-Herrero, Robust superconductivity in magic-angle multilayer graphene family, Nat. Mater. 21, 877 (2022).

[11] D. Guerci, P. Simon, and C. Mora, Higher-order Van Hove singularity in magic-angle twisted trilayer graphene, Phys. Rev. Res. 4, L012013 (2022).

[12] Y. Cao, D. Chowdhury, D. Rodan-Legrain, O. Rubies-Bigorda, K. Watanabe, T. Taniguchi, T. Senthil, and P. Jarillo-Herrero, Strange metal in magic-angle graphene with near planckian dissipation, Phys. Rev. Lett. 124, 076801 (2020).

[13] L. Wei, Q. Xu, Y. He, Q. Li, Y. Huang, W. Zhu, K. Watanabe, T. Taniguchi, M. Claassen, D. A. Rhodes, D. M. Kennes, L. Xian, A. Rubio, and L. Wang, Linear resistivity at van Hove singularities in twisted bilayer WSe_2, Proceedings of the National Academy of Sciences 121, e2321665121 (2024).

[14] H. Isobe and L. Fu, Supermetal, Phys. Rev. Res. 1, 033206 (2019).

[15] A. Chandrasekaran, A. Shtyk, J. J. Betouras, and C. Chamon, Catastrophe theory classification of Fermi surface topological transitions in two dimensions, Phys. Rev. Res. 2, 013355 (2020).

[16] N. F. Q. Yuan and L. Fu, Classification of critical points in energy bands based on topology, scaling, and symmetry, Phys. Rev. B 101, 125120 (2020).

[17] A. Chandrasekaran and J. J. Betouras, Effect of disorder on density of states and conductivity in higher-order Van Hove singularities in two-dimensional bands, Phys. Rev. B 105, 075144 (2022).

[18] A. Chandrasekaran and J. J. Betouras, A Practical Method to Detect, Analyze, and Engineer Higher Order Van Hove Singularities in Multi-band Hamiltonians, Advanced Physics Research 2, 2200061 (2023).

[19] E. H. Lieb, Two theorems on the Hubbard model, Phys. Rev. Lett. 62, 1201 (1989).

[20] A. J. Kollár, M. Fitzpatrick, P. Sarnak, and A. A. Houck, Line-graph lattices: Euclidean and non-euclidean flat bands, and implementations in circuit quantum electrodynamics, Communications in Mathematical Physics 376, 1909 (2020).

[21] D.-S. Ma, Y. Xu, C. S. Chiu, N. Regnault, A. A. Houck, Z. Song, and B. A. Bernevig, Spin-orbit-induced topological flat bands in line and split graphs of bipartite lattices, Phys. Rev. Lett. 125, 266403 (2020).

[22] B. R. Ortiz, L. C. Gomes, J. R. Morey, M. Winiarski, M. Bordelon, J. S. Mangum, I. W. H. Oswald, J. A. Rodriguez-Rivera, J. R. Neilson, S. D. Wilson, E. Ertekin, T. M. McQueen, and E. S. Toberer, New kagome prototype materials: discovery of KV_3Sb_5, RbV_3Sb_5, and CsV_3Sb_5, Phys. Rev. Mater. 3, 094407 (2019).

[23] M. Kang, S. Fang, J.-K. Kim, B. R. Ortiz, S. H. Ryu, J. Kim, J. Yoo, G. Sangiovanni, D. Di Sante, B.-G. Park,

[24] C. Jozwiak, A. Bostwick, E. Rotenberg, E. Kaxiras, S. D. Wilson, J.-H. Park, and R. Comin, Twofold van Hove singularity and origin of charge order in topological kagome superconductor CsV_3Sb_5, Nat. Phys. **18**, 301 (2022).

[24] S.-W. Kim, H. Oh, E.-G. Moon, and Y. Kim, Monolayer Kagome metals AV_3Sb_5, Nat. Commun. **14**, 591 (2023).

[25] Y. Luo, Y. Han, J. Liu, H. Chen, Z. Huang, L. Huai, H. Li, B. Wang, J. Shen, S. Ding, Z. Li, S. Peng, Z. Wei, Y. Miao, X. Sun, Z. Ou, Z. Xiang, M. Hashimoto, D. Lu, Y. Yao, H. Yang, X. Chen, H.-J. Gao, Z. Qiao, Z. Wang, and J. He, A unique van Hove singularity in kagome superconductor $CsV_{3-x}Ta_xSb_5$ with enhanced superconductivity, Nat. Commun. **14**, 3819 (2023).

[26] H. Li, S. Cheng, B. R. Ortiz, H. Tan, D. Werhahn, K. Zeng, D. Johrendt, B. Yan, Z. Wang, S. D. Wilson, and I. Zeljkovic, Electronic nematicity without charge density waves in titanium-based kagome metal, Nat. Phys. **19**, 1591 (2023).

[27] H. Yang, Y. Ye, Z. Zhao, J. Liu, X.-W. Yi, Y. Zhang, H. Xiao, J. Shi, J.-Y. You, Z. Huang, B. Wang, J. Wang, H. Guo, X. Lin, C. Shen, W. Zhou, H. Chen, X. Dong, G. Su, Z. Wang, and H.-J. Gao, Superconductivity and nematic order in a new titanium-based kagome metal $CsTi_3Bi_5$ without charge density wave order, Nat. Commun. **15**, 9626 (2024).

[28] L. Ye, M. Kang, J. Liu, F. von Cube, C. R. Wicker, T. Suzuki, C. Jozwiak, A. Bostwick, E. Rotenberg, D. C. Bell, L. Fu, R. Comin, and J. G. Checkelsky, Massive dirac fermions in a ferromagnetic kagome metal, Nature **555**, 638 (2018).

[29] J. Yin, W. Ma, T. A. Cochran, X. Xu, S. S. Zhang, H.-J. Tien, N. Shumiya, G. Cheng, K. Jiang, B. Lian, Z. Song, G. Chang, I. Belopolski, D. Multer, M. Litskevich, Z.-J. Cheng, X. P. Yang, B. Swidler, H. Zhou, H. Lin, T. Neupert, Z. Wang, N. Yao, T.-R. Chang, S. Jia, and M. Zahid Hasan, Quantum-limit Chern topological magnetism in $TbMn_6Sn_6$, Nature **583**, 533 (2020).

[30] M. Li, Q. Wang, G. Wang, Z. Yuan, W. Song, R. Lou, Z. Liu, Y. Huang, Z. Liu, H. Lei, Z. Yin, and S. Wang, Dirac cone, flat band and saddle point in kagome magnet YMn_6Sn_6, Nat. Commun. **12**, 3129 (2021).

[31] L. Wang, E.-M. Shih, A. Ghiotto, L. Xian, D. A. Rhodes, C. Tan, M. Claassen, D. M. Kennes, Y. Bai, B. Kim, K. Watanabe, T. Taniguchi, X. Zhu, J. Hone, A. Rubio, A. N. Pasupathy, and C. R. Dean, Correlated electronic phases in twisted bilayer transition metal dichalcogenides, Nat. Mater. **19**, 861 (2020).

[32] T. Devakul, V. Crépel, Y. Zhang, and L. Fu, Magic in twisted transition metal dichalcogenide bilayers, Nat. Commun. **12**, 6730 (2021).

[33] C. G. Péterfalvi, A. David, P. Rakyta, G. Burkard, and A. Kormányos, Quantum interference tuning of spin-orbit coupling in twisted van der Waals trilayers, Phys. Rev. Res. **4**, L022049 (2022).

[34] A. Veneri, D. T. S. Perkins, C. G. Péterfalvi, and A. Ferreira, Twist angle controlled collinear Edelstein effect in van der Waals heterostructures, Phys. Rev. B **106**, L081406 (2022).

[35] L. Sun, L. Rademaker, D. Mauro, A. Scarfato, A. Pásztor, I. Gutiérrez-Lezama, Z. Wang, J. Martinez-Castro, A. F. Morpurgo, and C. Renner, Determining spin-orbit coupling in graphene by quasiparticle interference imaging, Nat. Commun. **14**, 3771 (2023).

[36] Q. Rao, W.-H. Kang, H. Xue, Z. Ye, X. Feng, K. Watanabe, T. Taniguchi, N. Wang, M.-H. Liu, and D.-K. Ki, Ballistic transport spectroscopy of spin-orbit-coupled bands in monolayer graphene on WSe_2, Nat. Commun. **14**, 6124 (2023).

[37] D. T. S. Perkins, A. Veneri, and A. Ferreira, Spin hall effect: Symmetry breaking, twisting, and giant disorder renormalization, Phys. Rev. B **109**, L241404 (2024).

[38] H. Yang, B. Martín-García, J. Kimák, E. Schmoranzerová, E. Dolan, Z. Chi, M. Gobbi, P. Němec, L. E. Hueso, and F. Casanova, Twist-angle-tunable spin texture in WSe_2/graphene van der Waals heterostructures, Nat. Mater. **23**, 1502–1508 (2024).

[39] A. Abouelkomsan, E. J. Bergholtz, and S. Chatterjee, Multiferroicity and topology in twisted transition metal dichalcogenides, Phys. Rev. Lett. **133**, 026801 (2024).

[40] N. Regnault, Y. Xu, M.-R. Li, D.-S. Ma, M. Jovanovic, A. Yazdani, S. S. P. Parkin, C. Felser, L. M. Schoop, N. P. Ong, R. J. Cava, L. Elcoro, Z.-D. Song, and B. A. Bernevig, Catalogue of flat-band stoichiometric materials, Nature **603**, 824 (2022).

[41] M. G. Yamada, T. Soejima, N. Tsuji, D. Hirai, M. Dincă, and H. Aoki, First-principles design of a half-filled flat band of the kagome lattice in two-dimensional metal-organic frameworks, Phys. Rev. B **94**, 081102 (2016).

[42] T. Takenaka, K. Ishihara, M. Roppongi, Y. Miao, Y. Mizukami, T. Makita, J. Tsurumi, S. Watanabe, J. Takeya, M. Yamashita, K. Torizuka, Y. Uwatoko, T. Sasaki, X. Huang, W. Xu, D. Zhu, N. Su, J.-G. Cheng, T. Shibauchi, and K. Hashimoto, Strongly correlated superconductivity in a copper-based metal-organic framework with a perfect kagome lattice, Science Advances **7**, eabf3996 (2021).

[43] B. Field, A. Schiffrin, and N. V. Medhekar, Correlation-induced magnetism in substrate-supported 2d metal-organic frameworks, npj Computational Materials **8**, 227 (2022).

[44] S. Kang and J. Yu, Electronic structure and magnetic properties of transition metal kagome metal–organic frameworks, Phys. Chem. Chem. Phys. **24**, 22168 (2022).

[45] B. Lowe, B. Field, J. Hellerstedt, J. Ceddia, H. L. Nourse, B. J. Powell, N. V. Medhekar, and A. Schiffrin, Local gate control of Mott metal-insulator transition in a 2D metal-organic framework, Nat. Commun. **15**, 3559 (2024).

[46] Y. Xia, Z. Han, K. Watanabe, T. Taniguchi, J. Shan, and K. F. Mak, Superconductivity in twisted bilayer WSe_2, Nature (2024).

[47] M. Fuchs, P. Liu, T. Schwemmer, G. Sangiovanni, R. Thomale, C. Franchini, and D. Di Sante, Kagome metal-organic frameworks as a platform for strongly correlated electrons, J. Phys. Mater. **3**, 025001 (2020).

[48] A. Consiglio, T. Schwemmer, X. Wu, W. Hanke, T. Neupert, R. Thomale, G. Sangiovanni, and D. Di Sante, Van Hove tuning of AV_3Sb_5 kagome metals under pressure and strain, Phys. Rev. B **105**, 165146 (2022).

[49] F. Crasto de Lima, R. H. Miwa, and E. Suárez Morell, Double flat bands in kagome twisted bilayers, Phys. Rev. B **100**, 155421 (2019).

[50] T. Neupert, M. M. Denner, J.-X. Yin, R. Thomale, and M. Z. Hasan, Charge order and superconductivity in kagome materials, Nature Physics **18**, 137 (2022).

[51] P. Fontana, M. Burrello, and A. Trombettoni, Topological van Hove singularities at phase transitions in Weyl metals, Phys. Rev. B **104**, 195127 (2021).

[52] E. Wang, L. Pullasseri, and L. H. Santos, Higher-order Van Hove singularities in kagome topological bands, Phys. Rev. B **111**, 075114 (2025).

[53] D. T. S. Perkins, Symmetry presevation in commensurate twisted bilayers (2025), arXiv:2502.03106 [cond-mat.mes-hall].

[54] E. J. Mele, Commensuration and interlayer coherence in twisted bilayer graphene, Phys. Rev. B **81**, 161405 (2010).

[55] See the Supplemental Material where we show how the two classes of moiré patterns are related via reflection in $y = x$, as well as provide a summary of the Hamiltonian and electronic structure for monolayer and bilayer Kagomé. We also provide a derivation of the momentum space Hamiltonian from the real-space tight-binding Hamiltonian for any commensurate twist angle, and demonstrate how the choice of stacking can greatly influence the electronic structure and topology. We present further examples of the various HOVHSs that may be engineered in TBK for both topologically trivial and non-trivial cases. We also provide details behind our numerical calculation of the Chern numbers which required large grid sizes to accurately capture narrow avoided crossings. The Supplemental Material includes [71] as an additional reference.

[56] Y. Sheffer, R. Queiroz, and A. Stern, Symmetries as the guiding principle for flattening bands of dirac fermions, Phys. Rev. X **13**, 021012 (2023).

[57] H.-M. Guo and M. Franz, Topological insulator on the kagome lattice, Phys. Rev. B **80**, 113102 (2009).

[58] R. Ciola, K. Pongsangangan, R. Thomale, and L. Fritz, Chiral symmetry breaking through spontaneous dimerization in kagomé metals, Phys. Rev. B **104**, 245138 (2021).

[59] S. Regmi, A. P. Sakhya, T. Fernando, Y. Zhao, D. Jeff, M. Sprague, F. Gonzalez, I. Bin Elius, M. I. Mondal, N. Valadez, D. Jarrett, A. Agosto, J. Yang, J.-H. Chu, S. I. Khondaker, X. Xu, T. Cao, and M. Neupane, Observation of flat and weakly dispersing bands in the van der Waals semiconductor Nb_3Br_8 with breathing kagome lattice, Phys. Rev. B **108**, L121404 (2023).

[60] H. Zhang, Z. Shi, Z. Jiang, M. Yang, J. Zhang, Z. Meng, T. Hu, F. Liu, L. Cheng, Y. Xie, J. Zhuang, H. Feng, W. Hao, D. Shen, and Y. Du, Topological Flat Bands in 2D Breathing-Kagome Lattice Nb_3TeCl_7, Advanced Materials **35**, 2301790 (2023).

[61] F. D. M. Haldane, Model for a quantum hall effect without landau levels: Condensed-matter realization of the "parity anomaly", Phys. Rev. Lett. **61**, 2015 (1988).

[62] S. Shallcross, S. Sharma, and O. A. Pankratov, Quantum interference at the twist boundary in graphene, Phys. Rev. Lett. **101**, 056803 (2008).

[63] S. Shallcross, S. Sharma, E. Kandelaki, and O. A. Pankratov, Electronic structure of turbostratic graphene, Phys. Rev. B **81**, 165105 (2010).

[64] M. G. Scheer, K. Gu, and B. Lian, Magic angles in twisted bilayer graphene near commensuration: Towards a hypermagic regime, Phys. Rev. B **106**, 115418 (2022).

[65] V. C. Stangier, E. Berg, and J. Schmalian, Breakdown of the Wiedemann-Franz law at the Lifshitz point of strained Sr_2RuO_4, Phys. Rev. B **105**, 115113 (2022).

[66] A. Shtyk, G. Goldstein, and C. Chamon, Electrons at the monkey saddle: A multicritical lifshitz point, Phys. Rev. B **95**, 035137 (2017).

[67] A. Zervou, D. V. Efremov, and J. J. Betouras, Fate of density waves in the presence of a higher-order van Hove singularity, Phys. Rev. Res. **5**, L042006 (2023).

[68] M. L. Kiesel and R. Thomale, Sublattice interference in the kagome Hubbard model, Phys. Rev. B **86**, 121105 (2012).

[69] G. Galeotti, F. De Marchi, E. Hamzehpoor, O. MacLean, M. Rajeswara Rao, Y. Chen, L. V. Besteiro, D. Dettmann, L. Ferrari, F. Frezza, P. M. Sheverdyaeva, R. Liu, A. K. Kundu, P. Moras, M. Ebrahimi, M. C. Gallagher, F. Rosei, D. F. Perepichka, and G. Contini, Synthesis of mesoscale ordered two-dimensional π-conjugated polymers with semiconducting properties, Nat. Mater. **19**, 874 (2020).

[70] R. Pawlak, X. Liu, S. Ninova, P. D'Astolfo, C. Drechsel, J.-C. Liu, R. Häner, S. Decurtins, U. Aschauer, S.-X. Liu, and E. Meyer, On-surface synthesis of nitrogen-doped kagome graphene, Angewandte Chemie International Edition **60**, 8370 (2021).

[71] T. Fukui, Y. Hatsugai, and H. Suzuki, Chern numbers in discretized brillouin zone: Efficient method of computing (spin) hall conductances, J. Phys. Soc. Jpn **74**, 1674 (2005).

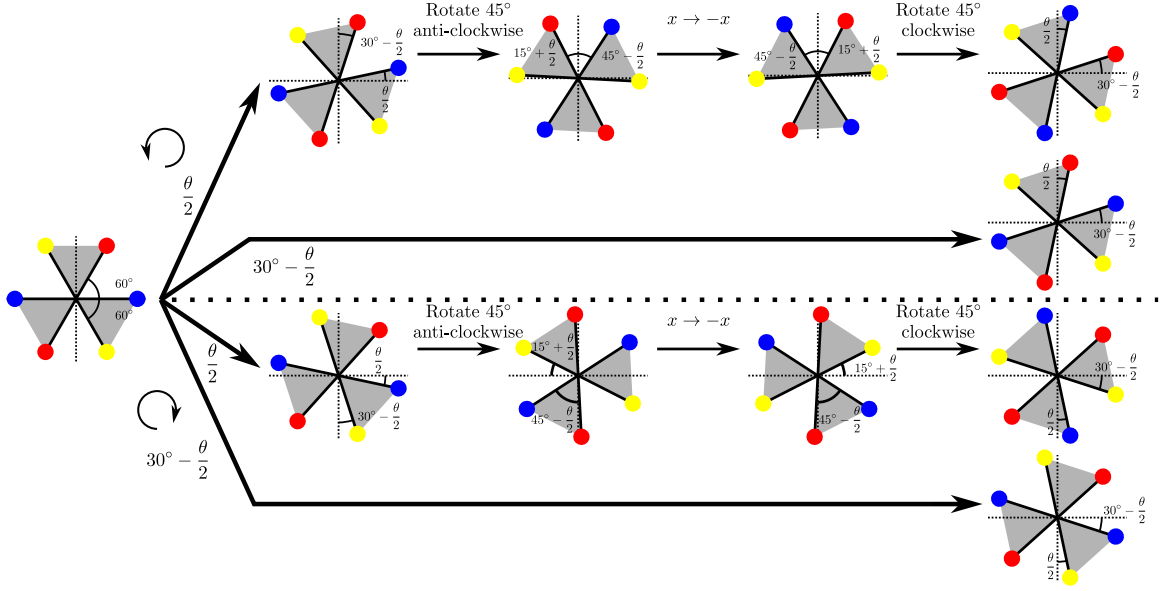[72] A. Chandrasekaran, In preparation.

FIG. 6. Schematic representation for the relation of layers rotated by an arbitrary angle of $\theta/2$ and $\theta'/2 = \pi/6 - \theta/2$ by reflection in the line of $y = x$. We start with the hexagon centre of a Kagomé lattice at the origin and label the three sublattices using red, blue, and yellow coloured dots. We connect these to the origin and shade down triangles whilst leaving up triangles blank. The first line shows the hexagon rotated anti-clockwise by $\theta/2$ and then transformed by reflection in $y = x$. The second line shows the hexagon rotated anti-clockwise by $\theta'/2$. Similarly, the third line shows the hexagon rotated clockwise by $\theta/2$ and then transformed by reflection in $y = x$, whilst the fourth line shows the hexagon rotated clockwise by $\theta'/2$.

SUPPLEMENTAL MATERIAL FOR "DESIGNING TOPOLOGICAL HIGH-ORDER VAN HOVE SINGULARITIES: TWISTED BILAYER KAGOMÉ"

VI.   TWO CLASSES OF MOIRÉ SUPERLATTICES

The set of commensurate angles are defined by a pair of unique coprime integers (m, n), such that $m > n > 0$. The commensurate angle θ_c associated to (m, n) is given by eq. 1 of the main text. These commensurate angles can be split into two classes: those with n divisible by 3 and those with n not divisible by 3. If θ_c is defined by a choice of n that is divisible by 3, then it has a partner commensurate angle that is associated to a choice of n that is not divisible by 3, $\theta'_c = \pi/3 - \theta_c$ [64]. When constructing a commensurate twisted bilayer we may choose to work in the twist-symmetric frame where layer 1 is rotated clockwise by $\theta_c/2$ and layer 2 is rotated anti-clockwise by $\theta_c/2$. We can relate the two classes of superlattices in the yielded by θ_c and θ'_c in the twist-symmetric frame by reflection in the line of $y = x$, as we prove below.

Let us start by considering a Kagomé hexagon centred on the origin and label each of the sublattices around the corners, see the first line of Fig. 6. We can choose to rotate this layer anti-clockwise by $\theta_c/2$ to acquire one of its orientations in the twist-symmetric frame for one of the superlattice classes. To reflect this in the line of $y = x$, we rotate the who system anti-clockwise by 45°, reflect it in the y-axis ($x \to -x$), and then rotate the system clockwise by 45°, as illustrated in Fig. 6. The other superlattice class would be given by choosing to rotate this layer by $\theta'_c/2 = (\pi/3 - \theta_c)/2$ anti-clockwise, see the second line of Fig. 6. By comparing the first and second lines of Fig. 6, we immediately see that the θ_c moiré pattern is mapped onto the θ'_c moire pattern with a swapping of sublattices. From the perspective of geometry there is no difference, but for the Hamiltonian this can have consequences due to the relative orientation of the sublattices determining the topological contribution.

Alternatively, we can instead choose to rotate this layer clockwise by either $\theta_c/2$ or $\theta'_c/2$ to consider the other layer in the twisted bilayer, as shown in the third and fourth lines of Fig. 6, respectively. By transforming $\theta_c/2$ layer by reflection in line of $y = x$, see the third line of Fig. 6, we again acquire the same geometry as the $\theta'_c/2$ layer. However, unlike the anti-clockwise rotation, not only is there a swapping of sublattices, but the orientation of up and down triangles is also swapped, as shown by the switching of highlighted and blank regions in Fig. 6. Therefore, whilst the geometry of the two classes are connected by a simple reflection, the topological aspect of the Hamiltonian we once again by flipped and the nature of dimersation will also be reversed.
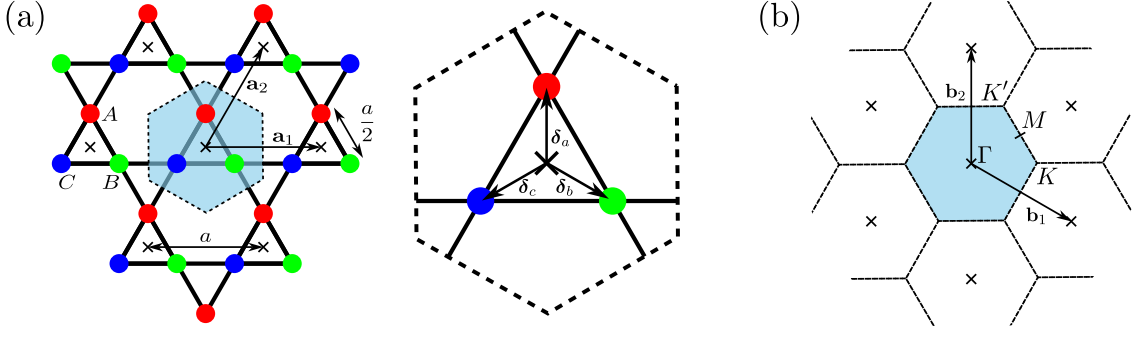
FIG. 7. (a): Kagome lattice structure with the lattice vectors, lattice sites (crosses), sublattices, and unit cell (shaded region) identified. (b): Reciprocal lattice of the Kagome lattice with the reciprocal lattice points marked by crosses. Wigner-Seitz unit cells are marked by dotted lines and the first Brillouin zone is shaded.

VII.   MONOLAYER KAGOME

To introduce conventions and help familiarise ourselves with the Kagome system, let us briefly recap the the monolayer Kagome system. We present a schematic of the Kagome lattice, Brillouin zone (BZ), and (reciprocal) lattice vectors in Fig. 7. The lattice vectors and sublattice positions are taken to be

$$\mathbf{a}_1 = a \begin{pmatrix} 1 \\ 0 \end{pmatrix}, \quad \mathbf{a}_2 = \frac{a}{2} \begin{pmatrix} 1 \\ \sqrt{3} \end{pmatrix}, \quad \boldsymbol{\delta}_a = \frac{a}{2\sqrt{3}} \begin{pmatrix} 0 \\ 1 \end{pmatrix}, \quad \boldsymbol{\delta}_b = \frac{a}{4\sqrt{3}} \begin{pmatrix} \sqrt{3} \\ -1 \end{pmatrix}, \quad \boldsymbol{\delta}_c = \frac{a}{4\sqrt{3}} \begin{pmatrix} -\sqrt{3} \\ -1 \end{pmatrix}, \tag{12}$$

with the origin set as the centre of an up triangle. The corresponding reciprocal lattice vectors are then

$$\mathbf{b}_1 = \frac{2\pi}{\sqrt{3}a} \begin{pmatrix} \sqrt{3} \\ -1 \end{pmatrix}, \qquad \mathbf{b}_2 = \frac{4\pi}{\sqrt{3}a} \begin{pmatrix} 0 \\ 1 \end{pmatrix}. \tag{13}$$

The tight binding Hamiltonian for the Kagome lattice with a single orbital per site, assuming constant nearest-neighbour tunneling, is simply

$$
\begin{aligned}
H &= -t \sum_i \left[(b_i^\dagger + c_i^\dagger) a_i + c_i^\dagger b_i \right] - t \sum_{\langle i,j \rangle}' \left[(b_j^\dagger + c_j^\dagger) a_i + c_j^\dagger b_i \right] + h.c. \\
&= -t \sum_i \sum_{\eta \neq \chi} \eta_i^\dagger \chi_i - t \sum_{\langle i,j \rangle}' \sum_{\eta \neq \chi} \eta_j^\dagger \chi_i, \qquad \chi, \eta \in \{a,b,c\},
\end{aligned}
\tag{14}
$$

where t is the tunneling energy, $\eta_i^\dagger$ and $\chi_i^\dagger$ are creation operators for sublattice η and χ, respectively, for the unit cell located at $\mathbf{R}_i$, η_i and χ_i are the corresponding annihilation operators, $\langle i,j \rangle$ denotes nearest-neighbour unit cells, and the primed sum indicates the restriction of the sum to ensure the sublattice sites are nearest-neighbours. We move to momentum space by performing a change of basis for the creation and annihilation operators,

$$\eta_i = \frac{1}{\sqrt{N}} \sum_{\mathbf{k}} e^{i\mathbf{k} \cdot (\mathbf{R}_i + \boldsymbol{\delta}_\eta)} \eta_{\mathbf{k}}, \qquad \chi_i = \frac{1}{\sqrt{N}} \sum_{\mathbf{k}} e^{i\mathbf{k} \cdot (\mathbf{R}_i + \boldsymbol{\delta}_\chi)} \chi_{\mathbf{k}}, \tag{15}$$

in which N is the number of unit cells in the periodic system. Substituting these expressions into eq. 14 yields

$$H = -t \sum_{\mathbf{k}} \sum_{\eta \neq \chi} \gamma_{\eta\chi}(\mathbf{k}) \eta_{\mathbf{p}}^\dagger \chi_{\mathbf{k}}, \tag{16}$$

with $\gamma_{\eta\chi}(\mathbf{k}) = 2\cos(\mathbf{k} \cdot \boldsymbol{\delta}_{\eta\chi})$ being the structure factor connecting sublattices η and χ and $\boldsymbol{\delta}_{\eta\chi} = \boldsymbol{\delta}_\eta - \boldsymbol{\delta}_\chi$. Defining the 3-component annihilation operator $\psi_{\mathbf{k}} = (a_{\mathbf{k}}, b_{\mathbf{k}}, c_{\mathbf{k}})^T$, we may write the Hamiltonian compactly as $H = \sum_{\mathbf{k}} \psi_{\mathbf{k}}^\dagger H_{\mathbf{k}} \psi_{\mathbf{k}}$, where

$$H_{\mathbf{k}} = \begin{pmatrix} 0 & -t\gamma_{ab}(\mathbf{k}) & -t\gamma_{ac}(\mathbf{k}) \\ -t\gamma_{ab}(\mathbf{k}) & 0 & -t\gamma_{bc}(\mathbf{k}) \\ -t\gamma_{ac}(\mathbf{k}) & -t\gamma_{bc}(\mathbf{k}) & 0 \end{pmatrix}, \tag{17}$$

Finally, diagonlaising this Hamiltonian yields

$$E_0 = 2t, \qquad E_\pm(\mathbf{k}) = -t \left[1 \pm \sqrt{3 + 2\cos(2\mathbf{k} \cdot \boldsymbol{\delta}_{ab}) + 2\cos(2\mathbf{k} \cdot \boldsymbol{\delta}_{ac}) + 2\cos(2\mathbf{k} \cdot \boldsymbol{\delta}_{bc})} \right]. \tag{18}$$

A. Dimerisation

To introduce dimerisation into the Kagome lattice, we include an additional tunneling that enhances hopping along up triangles and reduces hopping via down triangles, see Fig. 1c of the main text. We achieve this by adding

$$H_1 = -t_1 \sum_i \left[(b_i^\dagger + c_i^\dagger)a_i + c_i^\dagger b_i \right] + t_1 {\sum_{\langle i,j \rangle}}' \left[(b_j^\dagger + c_j^\dagger)a_i + c_j^\dagger b_i \right] + h.c.$$
$$= -t_1 \sum_i \sum_{\eta \neq \chi} \eta_i^\dagger \chi_i + t_1 {\sum_{\langle i,j \rangle}}' \sum_{\eta \neq \chi} \eta_j^\dagger \chi_i. \tag{19}$$

to the bare monolayer Hamiltonian, H. Written in momentum space, this contributes

$$H_{1,\mathbf{k}} = it_1 \begin{pmatrix} 0 & -\tilde{\gamma}_{ab}(\mathbf{k}) & -\tilde{\gamma}_{ac}(\mathbf{k}) \\ \tilde{\gamma}_{ab}(\mathbf{k}) & 0 & -\tilde{\gamma}_{bc}(\mathbf{k}) \\ \tilde{\gamma}_{ac}(\mathbf{k}) & \tilde{\gamma}_{bc}(\mathbf{k}) & 0 \end{pmatrix}, \tag{20}$$

where $\tilde{\gamma}_{\eta\chi}(\mathbf{k}) = 2\sin(\mathbf{k} \cdot \boldsymbol{\delta}_{\eta\chi})$. The bands for the full Hamiltonian, $H + H_1$, are then just

$$E_0 = 2t, \qquad E_\pm(\mathbf{k}) = -t \pm \sqrt{3t^2 + 6t_1^2 + 2(t^2 - t_1^2)(\cos(2\mathbf{k} \cdot \boldsymbol{\delta}_{ab}) + \cos(2\mathbf{k} \cdot \boldsymbol{\delta}_{ac}) + \cos(2\mathbf{k} \cdot \boldsymbol{\delta}_{bc}))}. \tag{21}$$

Consequently, at the K point the Dirac cone becomes gapped, $E_\pm(\mathbf{K}) = -t \pm t_1$, similar to the inclusion of a mass term in the low-energy description of monolayer graphene.

B. Haldane-type Hopping

Choosing to instead include a complex next-nearest-neighbour tunneling mechanism [52], we define anti-clockwise tunneling to possess a phase factor of $e^{i\phi}$ and clockwise tunneling to possess $e^{-i\phi}$, see Fig. 1d of the main text. The Hamiltonian describing this process is

$$H_2 = -t_2 {\sum_{\langle i,j \rangle}}'' \left[e^{i\phi}(a_i^\dagger b_j + b_i^\dagger c_j + c_i^\dagger a_j) + h.c. \right] = -t_2 {\sum_{\langle i,j \rangle}}'' \sum_{\eta \neq \chi} e^{i\mathcal{S}_{\eta\chi}\phi} \eta_i^\dagger \chi_j, \tag{22}$$

where the double primed sum denotes restriction to ensure the sublattices are next-nearest-neighbour and $\mathcal{S}_{\eta\chi} = \pm 1$ determines the sign of the complex tunneling phase. By inspecting eq. 22, we see a cyclic permutation of the sublattices between the creation and annihilation operators that possess the same phase factor. We may therefore map the sublattice labels $\{A, B, C\} \rightarrow \{1, 2, 3\}$ to write the phase sign compactly in terms of the rank-3 Levi-Civita tensor,

$$\mathcal{S}_{\eta\chi} = \sum_{\alpha=1}^3 \varepsilon_{\eta\chi\alpha}. \tag{23}$$

Finally, moving to momentum space, we arrive at

$$H_{2,\mathbf{k}} = -t_2 \begin{pmatrix} 0 & e^{i\phi}\bar{\gamma}_{ab}(\mathbf{k}) & e^{-i\phi}\bar{\gamma}_{ac}(\mathbf{k}) \\ e^{-i\phi}\bar{\gamma}_{ab}(\mathbf{k}) & 0 & e^{i\phi}\bar{\gamma}_{bc}(\mathbf{k}) \\ e^{i\phi}\bar{\gamma}_{ac}(\mathbf{k}) & e^{-i\phi}\bar{\gamma}_{bc}(\mathbf{k}) & 0 \end{pmatrix}, \tag{24}$$

where $\bar{\gamma}_{ij}(\mathbf{k})$ is the bare monolayer structure factor shifted by an appropriate lattice vector,

$$\bar{\gamma}_{ab}(\mathbf{k}) = 2\cos(\mathbf{k} \cdot (\boldsymbol{\delta}_{ab} + \mathbf{a}_1)), \quad \bar{\gamma}_{ab}(\mathbf{k}) = 2\cos(\mathbf{k} \cdot (\boldsymbol{\delta}_{ac} - \mathbf{a}_1)), \quad \bar{\gamma}_{bc}(\mathbf{k}) = 2\cos(\mathbf{k} \cdot (\boldsymbol{\delta}_{bc} - \mathbf{a}_2)). \tag{25}$$

VIII. UNTWISTED BILAYER HAMILTONIANS

A. *AA* Kagome Bilayer

For this choice of stacking, we introduce the interlayer tunneling strength $t_\perp$ to characterise the energy scale associated to the coupling between the layers. The effective tight binding Hamiltonian can then be written as

$$H_{AA} = H_1 + H_2 + H_{T,AA}, \qquad H_{T,AA} = -t_\perp \sum_i \sum_\eta \left[\eta_{i,1}^\dagger \eta_{i,2} + \eta_{i,2}^\dagger \eta_{i,1} \right], \tag{26}$$

where $H_{1,2}$ are the isolated Kagome Hamiltonians for the first and second layers, respectively, $H_{T,AA}$ is the interlayer tunneling Hamiltonian, and $\eta_{i,\alpha}^{\dagger}$ ($\eta_{i,\alpha}$) creates (annihilates) an electron on sublattice η of the αth layer in the ith unit cell. Moving to momentum space we find in the basis $\psi_{\mathbf{k}} = (a_{1\mathbf{k}}, b_{1\mathbf{k}}, c_{1\mathbf{k}}, a_{2\mathbf{k}}, b_{2\mathbf{k}}, c_{2\mathbf{k}})^{\text{T}}$,

$$H_{\mathbf{k}}^{(AA)} = \begin{pmatrix} H_{\mathbf{k}}^{(1)} & H_T^{(AA)} \\ H_T^{(AA)} & H_{\mathbf{k}}^{(2)} \end{pmatrix}, \qquad H_T^{(AA)} = \begin{pmatrix} -t_\perp & 0 & 0 \\ 0 & -t_\perp & 0 \\ 0 & 0 & -t_\perp \end{pmatrix}. \tag{27}$$

Due to the momentum being 2D, the interlayer separation distance, $d_\perp$, does not appear explicitly in this Hamiltonian. The bands for the AA bilayer system are then found to simply be those of the monolayer system shifted by $\pm t_\perp$,

$$E_{0,\pm} = 2t \pm t_\perp, \qquad E_{\mu\nu} = -\mu t_\perp - t\left[1 + \nu\sqrt{3 + 2\cos(2\mathbf{k} \cdot \boldsymbol{\delta}_{ab}) + 2\cos(2\mathbf{k} \cdot \boldsymbol{\delta}_{ac}) + 2\cos(2\mathbf{k} \cdot \boldsymbol{\delta}_{bc})}\right], \tag{28}$$

where $\mu, \nu = \pm 1$ label the different dispersive bands, which are shown in Fig. 1b of the main text.

B. AB Kagome Bilayer

With the same notation as before, the only change in this case is that tunneling may only occur between the A and B sublattices of the two layers, meaning there will be no matrix elements connecting the C sites between layeres. The Hamiltonian for this system is then simply

$$H_{AB} = H_1 + H_2 + H_{T,AB}, \qquad H_{T,AB} = -t_\perp \sum_i \left[a_{i,1}^{\dagger}b_{i,2} + b_{i,1}^{\dagger}a_{i,2} + h.c.\right]. \tag{29}$$

Moving to momentum space, we find

$$H_{\mathbf{k}}^{(AB)} = \begin{pmatrix} H_{\mathbf{k}}^{(1)} & H_T^{(AB)} \\ H_T^{(AB)} & H_{\mathbf{k}}^{(2)} \end{pmatrix}, \qquad H_T^{(AB)} = \begin{pmatrix} 0 & -t_\perp & 0 \\ -t_\perp & 0 & 0 \\ 0 & 0 & 0 \end{pmatrix}, \tag{30}$$

The eigenvalues of this Hamiltonian cannot be found analytically and so we resort to numerical diagonalisation to obtain the band structure shown in Fig. 1b of the main text.

C. Interlocked Kagome Bilayer

In this scenario where no sublattice site of one layer is located directly above any sublattice of the other layer, we instead focus on the partial overlap between sublattices of the two layers. For example, the A sites of one layer will have a reduced tunneling to the B and C sites of the other layer compared to the AA and AB stacking choices. Let us denote this reduced tunneling energy by $\tilde{t}_\perp$. We may then write the tight binding Hamiltonian for this system as

$$H_{\text{Int}} = H_1 + H_2 + H_{T,\text{Int}}, \qquad H_{T,\text{Int}} = -\tilde{t}_\perp \sum_i \sum_l \sum_{\eta \neq \chi} \eta_{i,\bar{l}}^{\dagger}\chi_{i,l}, \tag{31}$$

where the sum over l is the sum over layers and $\bar{l}$ refers to the opposite choice of l (i.e. if $l = 1$ then $\bar{l} = 2$ and vice versa). Unlike the AA and AB bilayers, we find that moving to momentum space generates an additional momentum dependent matrix elements of the continuum Hamiltonian due to the offset of the sublattices of the two layers of the form $\Phi_{\eta\chi}(\mathbf{k}) = e^{-i\mathbf{k}\cdot\boldsymbol{\delta}_{\eta_1\chi_2}}$. The continuum Hamiltonian for this system can then be written compactly as

$$H_{\mathbf{k}}^{(\text{Int})} = \begin{pmatrix} H_{\mathbf{k}}^{(1)} & H_{T,\mathbf{k}}^{(\text{Int})} \\ H_{T,\mathbf{k}}^{(\text{Int})\dagger} & H_{\mathbf{k}}^{(2)} \end{pmatrix}, \qquad H_{T,\mathbf{k}}^{(\text{Int})} = \begin{pmatrix} 0 & -\tilde{t}_\perp\Phi_{ab}(\mathbf{k}) & -\tilde{t}_\perp\Phi_{ac}(\mathbf{k}) \\ -\tilde{t}_\perp\Phi_{ba}(\mathbf{k}) & 0 & -\tilde{t}_\perp\Phi_{bc}(\mathbf{k}) \\ -\tilde{t}_\perp\Phi_{ca}(\mathbf{k}) & -\tilde{t}_\perp\Phi_{cb}(\mathbf{k}) & 0 \end{pmatrix}. \tag{32}$$

As in the AB stacking case, we find ourselves again unable to obtain analytic expressions for the band structure of the interlocked bilayer and obtain the band structure shown in Fig. 1b of the main text numerically.
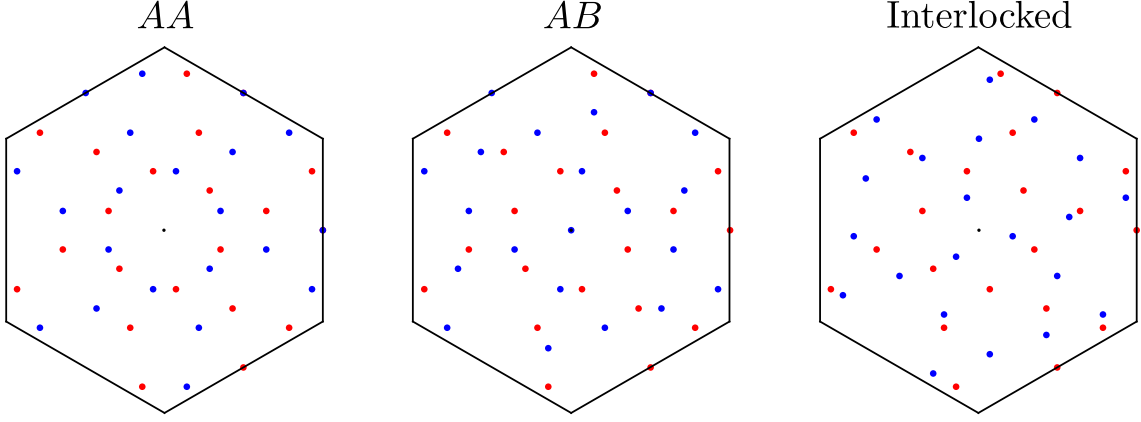
FIG. 8. Wigner-Seitz constructed moiré unit cells for the three possible stacking choices with a $\theta = 38.2°$ twist applied about the hexagon centre of layer 1. The red and blue dots belong to layers 1 and 2, respectively, whilst the small black dot indicates the twist origin and Wigner-Seitz lattice site. We show the MUCs in the twist symmetric frame.

IX. TBK TIGHT-BINDING HAMILTONIAN

Let us start by considering a Moire unit cell due to an arbitrary commensurate twist angle of θ_c. Each monolayer contributes N^{M} triangular lattice sites to the unit cell, and hence $3N^{\mathrm{M}}$ sublattice sites, thus leaving us with $6N^{\mathrm{M}}$ sublattice sites within the Moire unit cell. We may then introduce $c_{il\alpha}^{\dagger}$ ($c_{il\alpha}$) creation (annihilation) operators to describe the addition (removal) of an electron from sublattice α of layer l in the Moire unit cell centred on $\mathbf{R}_i$, where $\{\alpha \,|\, \alpha \in \mathbb{Z}, 1 \leq \alpha \leq 3N^{\mathrm{M}}\}$. We prescribe $\boldsymbol{\delta}_\alpha^{(l)}$ as the position of sublattice site α in layer l within the Moire unit cell. The general Hamiltonian for this system may then be written as

$$H = -\sum_i \sum_l \sum_{\alpha \neq \beta} t_{l,ii}^{\alpha\beta} c_{il\alpha}^{\dagger} c_{il\beta} - \sum_{\substack{\langle i,j\rangle, \\ \langle\langle i,j\rangle\rangle}} \sum_l \sum_{\alpha,\beta} t_{l,ij}^{\alpha\beta} c_{il\alpha}^{\dagger} c_{jl\beta}$$
$$- \sum_i \sum_{\alpha,\beta} t_{\perp,ii}^{\alpha\beta}(c_{i1\alpha}^{\dagger} c_{i2\beta} + c_{i2\beta}^{\dagger} c_{i1\alpha}) - \sum_{\substack{\langle i,j\rangle, \\ \langle\langle i,j\rangle\rangle}} \sum_{\alpha,\beta} t_{\perp,ij}^{\alpha\beta}(c_{i1\alpha}^{\dagger} c_{j2\beta} + c_{j2\beta}^{\dagger} c_{i1\alpha}),$$

(33)

assuming that the tunneling is real and decays sufficiently quickly to only allow tunneling up to next-nearest-neighbour Moire unit cells. The first line represents intralayer tunneling whilst the second line accounts for the interlayer tunneling. In writing this Hamiltonian, we noted that the tunneling energy should not depend on the direction of tunneling, $t_{\perp,ij}^{\alpha\beta} = t_{\perp,ji}^{\beta\alpha}$. Furthermore, we define the MUC as the Wigner-Seitz constructed unit cell centred on the twist origin, see Fig. 8, and use $\langle i,j\rangle$ and $\langle\langle i,j\rangle\rangle$ to denote nearest-neighbour and next-nearest-neighbour unit cells, respectively.

For simplicity, let us assume that the tunneling elements may be written as $t_{l,ij}^{\alpha\beta} = t^{\alpha\beta} f(|\mathbf{R}_i + \boldsymbol{\delta}_\alpha^{(l)} - \mathbf{R}_j - \boldsymbol{\delta}_\beta^{(l)}|)$ and $t_{\perp,ij}^{\alpha\beta} = t_{\perp 0}^{\alpha\beta} f_\perp(|\mathbf{R}_i + \boldsymbol{\delta}_\alpha^{(1)} - \mathbf{R}_j - \boldsymbol{\delta}_\beta^{(2)}|)$, with $t^{\alpha\beta} = t^{\beta\alpha}$ and $t_{\perp 0}^{\alpha\beta} = t_{\perp 0}^{\beta\alpha}$ (the superscripts remain to allow different orbital overlaps between sublattices), where $f(r)$ and $f_\perp(r)$ are functions that decay as r increases. Now we can move to momentum space,

$$H = -\sum_{\mathbf{k}} \sum_l \sum_{\alpha \neq \beta} t^{\alpha\beta} f(|\boldsymbol{\delta}_{\beta\alpha}^{(l)}|)e^{i\mathbf{k}\cdot\boldsymbol{\delta}_{\beta\alpha}^{(l)}} c_{\mathbf{k}l\alpha}^{\dagger} c_{\mathbf{k}l\beta} - \sum_{\mathbf{k}} \sum_l \sum_{\alpha,\beta} t^{\alpha\beta} \Gamma_l^{\alpha\beta}(\mathbf{k}) c_{\mathbf{k}l\alpha}^{\dagger} c_{\mathbf{k}l\beta}$$
$$- \sum_{\mathbf{k}} \sum_{\alpha,\beta} t_{\perp 0}^{\alpha\beta} f(|\boldsymbol{\delta}_{\beta\alpha}^{(21)}|)\left[e^{i\mathbf{k}\cdot\boldsymbol{\delta}_{\beta\alpha}^{(21)}} c_{\mathbf{k}1\alpha}^{\dagger} c_{\mathbf{k}2\beta} + e^{-i\mathbf{k}\cdot\boldsymbol{\delta}_{\beta\alpha}^{(21)}} c_{\mathbf{k}2\beta}^{\dagger} c_{\mathbf{k}1\alpha}\right]$$
$$- \sum_{\mathbf{k}} \sum_{\alpha,\beta} t_{\perp 0}^{\alpha\beta}\left[\Gamma_\perp^{\alpha\beta}(\mathbf{k}) c_{\mathbf{k}1\alpha}^{\dagger} c_{\mathbf{k}2\beta} + \Gamma_\perp^{\alpha\beta}(\mathbf{k})^* c_{\mathbf{k}2\beta}^{\dagger} c_{\mathbf{k}1\alpha}\right],$$

(34)

with $\boldsymbol{\delta}_{\beta\alpha}^{(l)} = \boldsymbol{\delta}_{\beta}^{(l)} - \boldsymbol{\delta}_{\alpha}^{(l)}$, $\boldsymbol{\delta}_{\beta\alpha}^{(21)} = \boldsymbol{\delta}_{\beta}^{(2)} - \boldsymbol{\delta}_{\alpha}^{(1)}$,

$$\Gamma_l^{\alpha\beta}(\mathbf{k}) = \sum_{i=1}^{18} f(|\boldsymbol{\delta}_{\beta\alpha}^{(l)} + \mathbf{c}_i^{\mathrm{M}}|)e^{i\mathbf{k}\cdot(\boldsymbol{\delta}_{\beta\alpha}^{(l)} + \mathbf{c}_i^{\mathrm{M}})}, \qquad \Gamma_\perp^{\alpha\beta}(\mathbf{k}) = \sum_{i=1}^{18} f_\perp(|\boldsymbol{\delta}_{\beta\alpha}^{(21)} + \mathbf{c}_i^{\mathrm{M}}|)e^{i\mathbf{k}\cdot(\boldsymbol{\delta}_{\beta\alpha}^{(21)} + \mathbf{c}_i^{\mathrm{M}})}, \tag{35}$$

and

$$\begin{aligned}\{\mathbf{c}_i^{\mathrm{M}}\} = \{ &\pm \mathbf{a}_1^{\mathrm{M}}, \pm\mathbf{a}_2^{\mathrm{M}}, \pm(\mathbf{a}_2^{\mathrm{M}} - \mathbf{a}_1^{\mathrm{M}}), \\ &\pm 2\mathbf{a}_1^{\mathrm{M}}, \pm 2\mathbf{a}_2^{\mathrm{M}}, \pm 2(\mathbf{a}_2^{\mathrm{M}} - \mathbf{a}_1^{\mathrm{M}}), \pm(\mathbf{a}_2^{\mathrm{M}} + \mathbf{a}_1^{\mathrm{M}}), \pm(2\mathbf{a}_2^{\mathrm{M}} - \mathbf{a}_1^{\mathrm{M}}), \pm(2\mathbf{a}_1^{\mathrm{M}} - \mathbf{a}_2^{\mathrm{M}})\},\end{aligned} \tag{36}$$

being the set of Moire lattice vectors connecting nearest-neighbour and next-nearest-neighbour Moire unit cells. We can further simplify the Hamiltonian in eq. 34 by introducing

$$\widetilde{\Gamma}_l^{\alpha\beta}(\mathbf{k}) = f(|\boldsymbol{\delta}_{\beta\alpha}^{(l)}|)e^{i\mathbf{k}\cdot\boldsymbol{\delta}_{\beta\alpha}^{(l)}}(1 - \delta_{\alpha\beta}) + \Gamma_l^{\alpha\beta}(\mathbf{k}), \qquad \widetilde{\Gamma}_\perp^{\alpha\beta}(\mathbf{k}) = f(|\boldsymbol{\delta}_{\beta\alpha}^{(21)}|)e^{i\mathbf{k}\cdot\boldsymbol{\delta}_{\beta\alpha}^{(21)}} + \Gamma_\perp^{\alpha\beta}(\mathbf{k}), \tag{37}$$

which yields

$$H = -\sum_{\mathbf{k}}\sum_l\sum_{\alpha,\beta} t^{\alpha\beta}\widetilde{\Gamma}_l^{\alpha\beta}(\mathbf{k})c_{\mathbf{k}l\alpha}^\dagger c_{\mathbf{k}l\beta} - \sum_{\mathbf{k}}\sum_{\alpha,\beta} t_{\perp 0}^{\alpha\beta}\left[\widetilde{\Gamma}_\perp^{\alpha\beta}(\mathbf{k})c_{\mathbf{k}1\alpha}^\dagger c_{\mathbf{k}2\beta} + \widetilde{\Gamma}_\perp^{\alpha\beta}(\mathbf{k})^* c_{\mathbf{k}2\beta}^\dagger c_{\mathbf{k}1\alpha}\right]. \tag{38}$$

We include complex next-nearest-neighbour tunneling as a purely intralayer process. Written in real space, this mechanism contributes

$$H_{\mathrm{H}} = -t_{\mathrm{H}}\sum_l\sum_i\sideset{}{''}\sum_{\alpha\neq\beta} e^{i\mathcal{S}_{\alpha\beta}\phi}c_{il\alpha}^\dagger c_{il\beta} - t_{\mathrm{H}}\sum_l\sum_{\langle i,j\rangle}\sideset{}{''}\sum_{\alpha,\beta} e^{i\mathcal{S}_{\alpha\beta}\phi}c_{il\alpha}^\dagger c_{jl\beta} \tag{39}$$

to the Hamiltonian, where the double primes indicate the restriction of the sum to next-nearest-neighbour sites. Moving to momentum space yields

$$H_{\mathrm{H}} = -t_{\mathrm{H}}\sum_{\mathbf{k}}\sum_l\sum_{\alpha,\beta}\Gamma_{\mathrm{H}}^{\alpha\beta}(\mathbf{k})e^{i\mathcal{S}_{\alpha\beta}\phi}c_{\mathbf{k}l\alpha}^\dagger c_{\mathbf{k}l\beta}, \tag{40}$$

with

$$\Gamma_{\mathrm{H}}^{\alpha\beta}(\mathbf{k}) = \left[\delta_{\langle\langle\alpha,\beta\rangle\rangle} + \sum_{i=1}^6 \delta_{\langle\langle\alpha,\beta\rangle\rangle}^i e^{i\mathbf{k}\cdot\mathbf{c}_i^{\mathrm{M}}}\right], \tag{41}$$

where $\delta_{\langle\langle\alpha,\beta\rangle\rangle}$ is unity when α and β are next-nearest-neighbours within the same unit cell and zero otherwise. Similarly, $\delta_{\langle\langle\alpha,\beta\rangle\rangle}^i$ is unity when α and β are next-nearest-neighbours whilst located in nearest-neighbour unit cells, such that their separation is $\boldsymbol{\delta}_\alpha - \boldsymbol{\delta}_\beta - \mathbf{c}_i^{\mathrm{M}}$, and zero otherwise.

X. COMPARISON OF TBK STRUCTURES

In the main text we saw that the band structure of TBK was sensitive to the choice of stacking order primarily around the K_{M} and M_{M} points outside of the near-flat band region in the absence of dimerisation and Haldane hopping. When either of these effects are introduced into the Hamiltonian we find that the various stacking choices start to exhibit clearer differences in their band structures, as shown in Fig. 9. The largest changes between the stacking orders are seen in the lower 14 bands (i.e. those below the MDP energy), especially about the M_{M} point, though notable differences can still be seen along the high-symmetry path between Γ_{M} and K_{M} and at the MBZ corners.

When dimerisation is introduced in all cases (Figs. 9a and 9b), we find that the relatively flat nature of the bands is preserved with the bands becoming slightly more dispersive and the width of the near-flat band region is increased. In particular, we see what appear to be two flat energy surfaces appearing in the twisted AA bilayer, reminiscent of the untiwsted case. However, upon closer inspection, we find this is not actually the case. For the uppermost band (band 42), we find it exhibits variations in energy on the scale of $\sim 10^{-3}t$. In contrast the lower apparently flat surface formed of two bands near $E = 1.86t$ exhibits an avoided crossing and not a degeneracy between the two bands the surface lies in. Moreover, we find a similarly weak momentum dependence yielding variations in energy on the scale of $\sim 10^{-4}t$. If we instead use an imaginary next-nearest-neighbour tunneling, as in Figs. 9c and 9d, we find that bands 41 and 42 become significantly more dispersive for all choices of stacking order. However, the choice of stacking can be seen to be crucial in whether or not an insulating gap opens and in the size of this gap. This suggests that the stacking order will play a central role in transport measurements of Hall conductance due to topologically protected edge states.
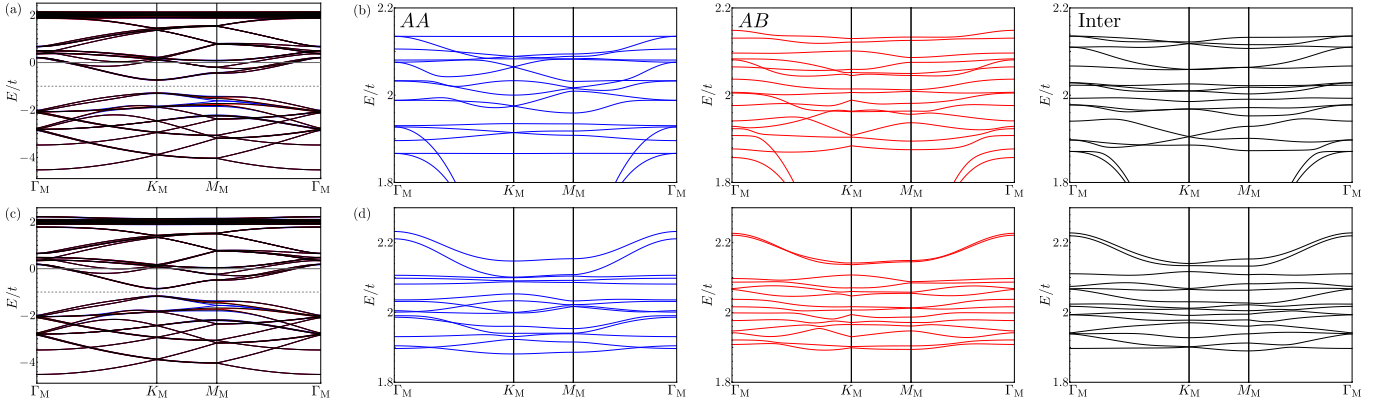
FIG. 9. Comparison of the band structures for the three high-symmetry stacking orders in the presence of dimerisation and Haldane hopping. (a): Complete band structure of all three stackings with $t_d = 0.1t$. (b): Near-flat band region of panel (a) for each stacking order. (c): Completed band structure of all three stackings with $t_\mathrm{H} = 0.05t$ and $\phi = \pi/2$. (d): Near-flat band region of panel (c) for each stacking order. In all cases above we have taken $\theta_c = 38.2°$, $a = 0.5338$ nm, $d_\perp = 0.6596$ nm, $t_\mathrm{H} = 0$, $\phi = 0$, $t_\perp = 0.3t$, $\gamma = 20$ [28, 49]. The grey dashed line indicates the MDP energy.

TABLE II. Summary of the approximate parameters yielding monkey saddle singularities in AA and interlocked TBK when either dimerisation of Haldane hopping is present. In all cases we take $\theta_c = 38.2°$, $a = 0.5338$ nm, $d_\perp = 0.6596$ nm, $t_\perp = 0.3t$, $\gamma = 20$ [28, 49]. The parameters listed here should be read as two sets: unbracketed values belong to AA TBK whilst bracketed values belong to interlocked TBK. The asterisk indicates the only case where an interlayer potential is present with $\Delta = 0.4t$.

	Dimerisation				Topological		
Band	t_d/t	Band	t_d/t	Band	t_H/t	Band	t_H/t
2	0.68 (0.7)	18	0.29 (0.402)	2	0.621 (0.66)	18	0.09595
5	0.5 (0.484)	21	0.179*	5	0.4859 (0.5172)	20	0.18147 (0.26589)
8	0.0862 (0.14)	25	0.51 (0.313)	8	0.0697 (0.122)	21	(0.0418)
11	0.05 (0.14)	26	0.44533 (0.525)	11	0.04498 (0.1188)	25	0.31251 (0.28619)
12	0.59 (0.3195)	–	–	12	(0.2102)	26	0.470977 (0.09825)

XI. MONKEY SADDLE SINGULARITIES

A. Dimerisation

We present further examples of monkey saddle singularities for both the AA and interlocked TBK systems to highlight the wide range of parameter choices that may be taken in engineering monkey saddles. Fig. 10 contains monkey saddles created through dimerisation of the Kagome lattice. Here we see that the choice of stacking order can significantly change the dimerisation required to obtain a singularity around the K_M point, as is the case for band 8 (Fig. 10a and Fig. 10e). Moreover, we find that an interlayer potential can act as an additional tuning knob to create monkey saddles at the MBZ corners, see Fig. 10b. We also observe that both localised and delocalised singularities manifest in other bands, highlighting that both can be found with relative ease. A list of the monkey saddles we have found TBK is given in Table II alongside the dimerisations and interlayer potentials required to engineer them.

B. Topological tunneling

As discussed in the main text, we may instead engineer the TBK band structure through the introduction of a complex next-nearest-neighbour hopping to create monkey saddle singularities. Here we present further examples of monkey saddle singularities that can be acquired in both AA and interlocked TBK through a purely imaginary Haldane tunneling term. Fig. 11 illustrates the range of values that may be taken for t_H and how monkey saddles can be acquired in several bands outside of the near-flat band region. We provide a list of the monkey saddle singularities we have found in TBK due to Haldane hopping in Table II.
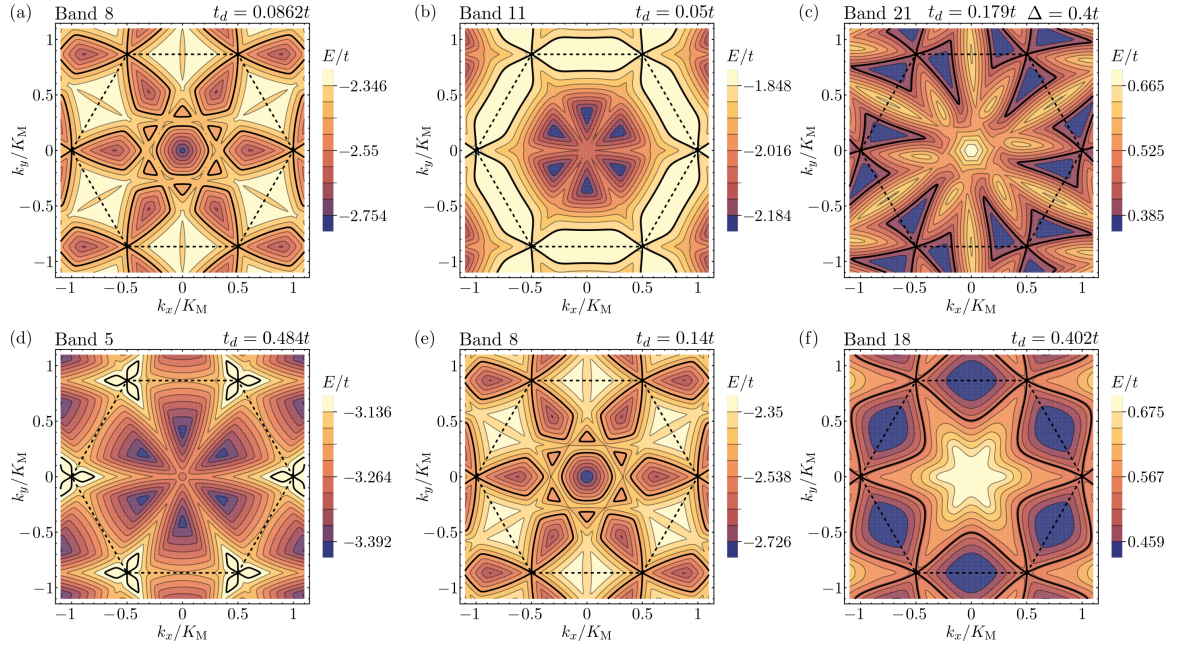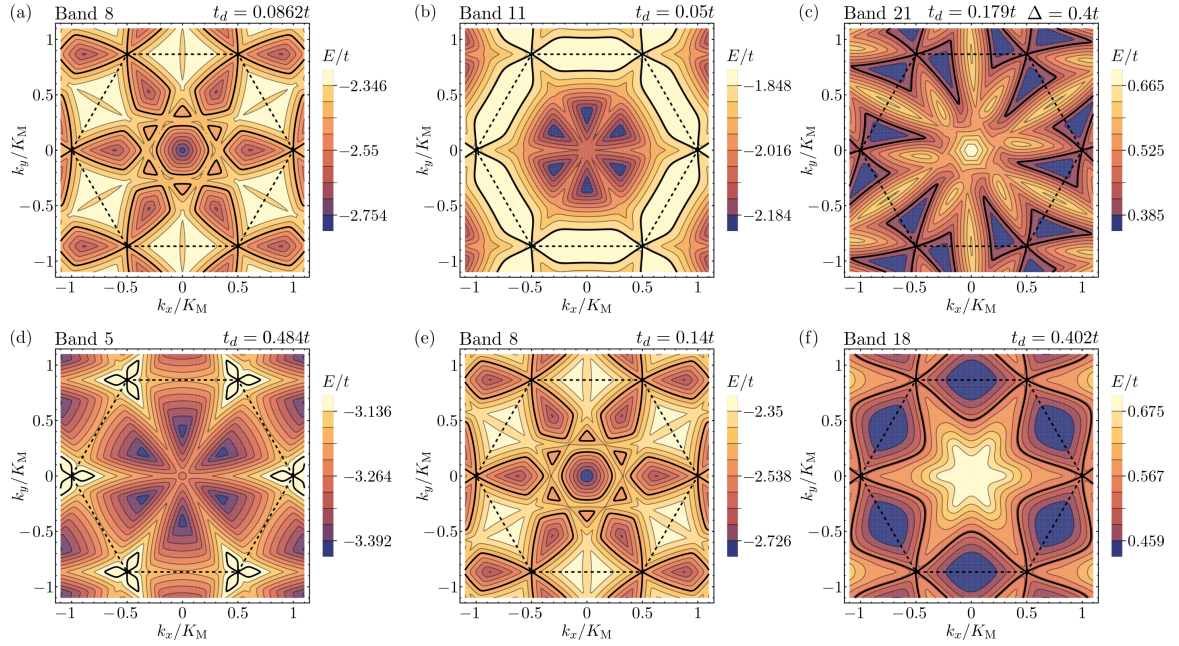
FIG. 10. (a)-(c): Monkey saddle singularities arising in *AA* TBK. (d)-(f): Monkey saddle singularities appearing in interlocked TBK. The band considered and choice of dimerisation is stated in each panel. Only in (c) is the interlayer potential taken to be non-zero, thus breaking the effective $k_y \rightarrow -k_y$ symmetry. The bold black lines denote the energy contour of the critical point, whilst the dashed line indicates the MBZ boundary. We take $\theta_c = 38.2°$, $a = 0.5338$ nm, $d_\perp = 0.6596$ nm, $t_{\mathrm{H}} = 0$, $\phi = 0$, $t_\perp = 0.3t$, $\gamma = 20$ [28, 49] for the system considered here.

FIG. 11. (a)-(c): Monkey saddle singularities arising in *AA* TBK. (d)-(f): Monkey saddle singularities appearing in interlocked TBK. The band considered and choice of Haldane hopping is stated in each panel. The bold black lines denote the energy contour of the critical point, whilst the dashed line indicates the MBZ boundary. We take $\theta_c = 38.2°$, $a = 0.5338$ nm, $d_\perp = 0.6596$ nm, $t_d = 0$, $\phi = \pi/2$, $t_\perp = 0.3t$, $\gamma = 20$ [28, 49] for the system considered here.

C.   Obtaining Monkey Saddle Singularities

The presence of a monkey saddle singularity can be determined by checking the vanishing of all second-order terms in the expansion of the band energy about the K_M point. Expanding a given band around the K_M point that hosts a critical point yields

$$\varepsilon = \varepsilon_0 + c_0^{(2)} p_x^2 + c_1^{(2)} p_x p_y + c_2^{(2)} p_y^2 + c_0^{(3)} p_x^3 + c_1^{(3)} p_x^2 p_y + c_2^{(3)} p_x p_y^2 + c_3^{(3)} p_y^3 + \mathcal{O}(p^4) \tag{42}$$

for the local dispersion where $\mathbf{p} = \mathbf{k} - \mathbf{K}_M$, $c_i^{(j)}$ are generic expansion constants, and ε_0 is the band's energy at the K_M point. A regular VHS will manifest when the second-order coefficients are non-zero. The point group symmetry of AA TBK is D_6 whilst for interlocked TBK it is D_3 [53]. When dimerisation is added they are both D_3. If an out-of-plane electric field is applied to induce an interlayer potential, then the dihedral symmetry is broken due to one layer acquiring an on-site energy of $\Delta/2$ and the other $-\Delta/2$, reducing the point group symmetry to C_{3z}. The three-fold rotational symmetry of this system ensures that the MBZ corners must also exhibit C_{3z} symmetry, requiring $c_0^{(2)} = c_2^{(2)}$, $c_2^{(3)} = -3c_0^{(3)}$, $c_1^{(3)} = -3c_3^{(3)}$, and $c_1^{(2)} = 0$, to yield

$$\varepsilon = \varepsilon_0 + c_0^{(2)} p^2 + p^3 [c_1^{(3)} \cos(3\varphi) - c_4^{(3)} \sin(3\varphi)] + \mathcal{O}(p^4), \tag{43}$$

where φ is the local azimuthal angle.

Let us now restrict the above scenario to one where dihedral symmetry is preserved (i.e. no interlayer potential). In this case, the dihedral symmetry manifests as a $k_y \to -k_y$ reflection symmetry in momentum space within the twist symmetric frame courtesy of the system's effective 2D nature: the dihedral symmetry can be thought of as a reflection in the x-axis ($y \to -y$) followed by a reflection in the xy plane ($z \to -z$ i.e. swapping the layers). The out-of-plane reflection has no effect on the dispersion since the layers are identical. Hence, dihedral symmetry sets $c_4^{(3)} = 0$, resulting in

$$\varepsilon = \varepsilon_0 + c_0^{(2)} p^2 + c_1^{(3)} p^3 \cos(3\varphi) + \mathcal{O}(p^4). \tag{44}$$

This effective $k_y \to -k_y$ is seen in all cases of Fig. 10, aside from Fig. 10c, where an interlayer potential is absent. Fig. 10c demonstrates how this effective reflection symmetry is broken through the application of an out-of-plane electric field. Nonetheless, whether dihedral symmetry is preserved or not, we can demonstrate the existance of an exact monkey saddle simply by studying how $c_0^{(2)}$ changes as the tuning parameters are varied. If $c_0^{(2)} = 0$ at some point whilst some third-order coefficients are non-zero, then that choice of parameters will yield a monkey saddle singularity. We present the dependence of $c_0^{(2)}$ on the dimerisation and Haldane hopping in Fig. 12 to illustrate this in various bands of AA and interlocked TBK.
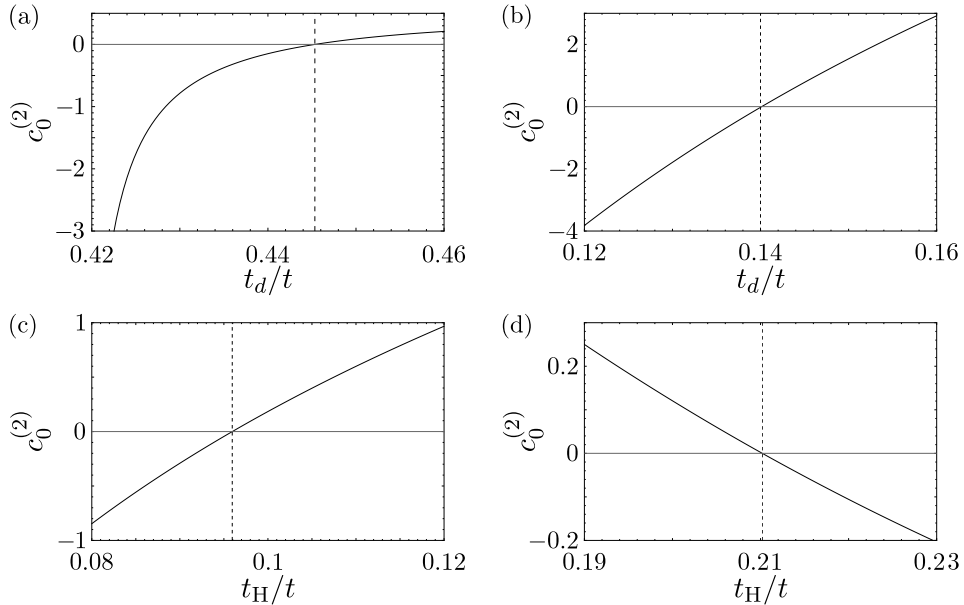

FIG. 12. Here we show how the second-order coefficient, $c_0^{(2)}$, varies with dimerisation and Haldane hopping. (a): band 26 with AA stacking. (b): band 8 with interlocked stacking. (c): band 18 with AA stacking. (d): band 12 with interlocked stacking.

D. Higher-Order Monkey Saddle Corrections to the DOS

The density of states (DOS) for a band with dispersion $E(\mathbf{k})$ is given by

$$g(\epsilon) = \int_{\text{BZ}} \frac{d^2 k}{(2\pi)^2} \, \delta(E(\mathbf{k}) - \epsilon), \tag{45}$$

where the integral is over the BZ. If $E(\mathbf{k})$ has the form of a pure HOVHS, we can obtain the power-law behaviour of the DOS by scaling $k_x \to |\epsilon|^\alpha p_x$ and $k_y \to |\epsilon|^\beta p_y$ for some appropriate α and β in this integral. For example, for the HOVHS $k_x^4 - k_y^2$, we need to set $\alpha = 1/4, \beta = 1/2$ so that

$$
\begin{aligned}
g(\epsilon) &\approx \int_{\mathbb{R}^2} \frac{d^2 k}{(2\pi)^2} \, \delta(k_x^4 - k_y^2 - \epsilon) \\
&= \int_{\mathbb{R}^2} \frac{|\epsilon|^{\frac{1}{4} + \frac{1}{2}} \, d^2 p}{(2\pi)^2} \, \delta(|\epsilon| p_x^4 - |\epsilon| p_y^2 - \epsilon) \\
&= |\epsilon|^{-\frac{1}{4}} \int_{\mathbb{R}^2} \frac{d^2 p}{(2\pi)^2} \, \delta(p_x^4 - p_y^2 - \text{sign}(\epsilon)) \\
&= D_\pm |\epsilon|^{-\frac{1}{4}},
\end{aligned}
\tag{46}
$$

where we have extended the integral over the entire real plane (introducing a finite error in comparison to the divergence of the DOS) and used the scaling property of the delta function: $\delta(ax) = \delta(x)/|a|$. The final integral is independent of the magnitude of ϵ and depends only on the sign, evaluating respectively to D_+ for $\epsilon > 0$ and D_- for $\epsilon < 0$. The ratio D_+/D_- is a characteristic feature of each HOVHS, alongside the exponent of the power-law DOS. In particular, the power-law DOS for the $k_x^4 - k_y^2$ singularity is $|\epsilon|^{-1/4}$. When there are higher-order terms that correct the HOVHS (as happens for the series expansion of a realistic band dispersion), we are guaranteed to have a smooth coordinate transformation with a smooth inverse $\psi : (\tilde{k}_x, \tilde{k}_y) \to (k_x, k_y)$ that maps the full dispersion to the exact form of the HOVHS in some neighbourhood of the critical point. That is, with $(k_x, k_y) = \psi(\tilde{k}_x, \tilde{k}_y)$ we have $E(k_x, k_y) = E(\psi(\tilde{k}_x, \tilde{k}_y)) = \tilde{k}_x^4 - \tilde{k}_y^4$ (or the equivalent form for the other HOVHS). The DOS integral then takes the form

$$g(\epsilon) \approx \int_{\mathbb{R}^2} \frac{d^2 \tilde{k}}{(2\pi)^2} \, J(\tilde{k}_x, \tilde{k}_y) \, \delta(\tilde{k}_x^4 - \tilde{k}_y^2 - \epsilon), \tag{47}$$

where $J(\tilde{k}_x, \tilde{k}_y)$ is the Jacobian determinant for ψ that is necessary to effect the change of variables in a multiple integral. Since ψ is a local diffeomorphism, $J_0 = J(0,0)$ has to be non-zero. We can then series expand $J(\tilde{k}_x, \tilde{k}_y)$ around $(0,0)$, scale $\tilde{k}_x$ and $\tilde{k}_y$ in each integral in the resultant series appropriately to obtain the power-law DOS at leading order, that is corrected by sub-leading terms [15]

$$g(\epsilon) \approx |\epsilon|^{-\gamma} \left(J_0 D_\pm + \sum_{n=1}^{\infty} \sum_{m=0}^{n} c_{mn} |\epsilon|^{m\alpha + (n-m)\beta} \right), \tag{48}$$

where the leading order exponent γ equals $1 - \alpha - \beta$. Since $0 < \alpha, \beta < 1$ and $m \leq n$, we have $m\alpha + (n-m)\beta > 0$, which ensures that terms in the sum are subleading in the $\epsilon \to 0$ limit. While fitting for the power law DOS arising from a realistic dispersion with HOVHS, we may have to include a few terms in this series to get an accurate description for the chosen energy range near the critical energy. Notice that the leading order terms for $\epsilon > 0$ and $\epsilon < 0$ respectively have the coefficients $J_0 D_+$ and $J_0 D_-$ ensuring that the universal ratio of prefactors D_+/D_- is preserved.
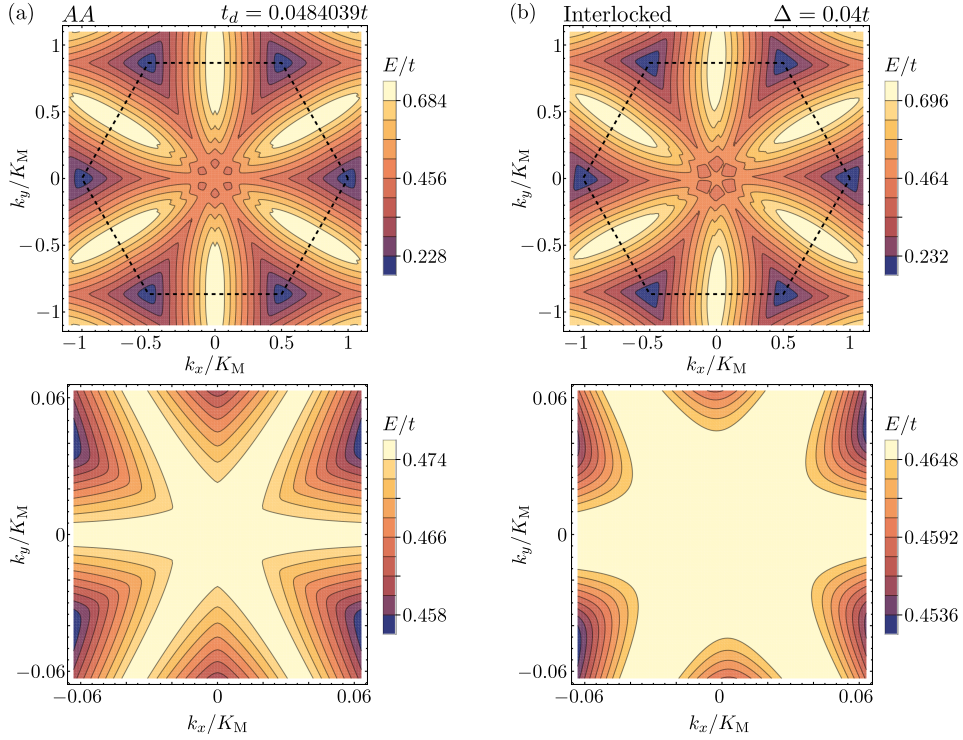
FIG. 13. Examples of effective sixth-order HOVHSs in in band 22 for AA (a) and interlocked (b) TBK. We take $\theta_c = 38.2°$, $a = 0.5338$ nm, $d_\perp = 0.6596$ nm, $t_H = 0$, $\phi = 0$, $t_\perp = 0.3t$, $\gamma = 20$ [28, 49].

XII. SIXTH-ORDER SINGULARITIES

Given the extremely sensitive nature of sixth-order VHSs, it is difficult to engineer the TBK band structure to host them with only a couple of tuning parameters. We present examples of effective sixth-order singularities appearing in band 22 for both AA and interlocked TBK in Fig. 13 using a single parameter. We find there to exists a small minimum for the interlocked stacking at Γ_M surrounded by set of of six closely packed second-order VHSs. The depth of this minimum relative to the saddle point energies of these surrounding singularities is $\sim 10^{-6}t$, suggesting that we should expect divergences in the DOS characteristic of a sixth-order singularity. However, for the AA configuration, we are unable to observe such a set of second-orders singularities as clearly and obtain a vanishingly small value for the second-order coefficient, $c_0^{(2)}$, in the expansion of the energy about the Γ_M point. Given the lack of a clear extremum in our calculations, see Fig. 13a, this suggests the system is tuned very close to an extended extremum [72], where the extremal value is not isolated to a single point but instead a set of connected points extending from the extremal point to infinity.

XIII. SECOND-ORDER SINGULARITIES

For completeness we present examples of the various two-fold symmetric HOVHSs in Fig. 14 for all three stacking choices. We see that TBK naturally hosts many such singularities without any need to tune the Hamiltonian, exhibiting both localised and delocalised singularities. Nonetheless, it is possible to engineer these second-order singularities through dimerisation, as illustrated by band 10 for interlocked TBK in Fig. 14b. We can therefore expect twisted breathing Kagome bilayer to host unique HOVHSs with 2-fold rotational symmetry that would not appear in the regular twisted bilayer. Interestingly, we find that band 4 for all stackings without dimerisation might be tunable to host a fourth-order singularity. Specifically, we find that it hosts a small minimum at the M_M point rather than a two-fold symmetric singularity. However, two second-order singularities lie nearby to both the M_M point and each other, see Fig. 15. It may therefore be possible to engineer a fourth-order singularity via other tuning parameters not considered here.
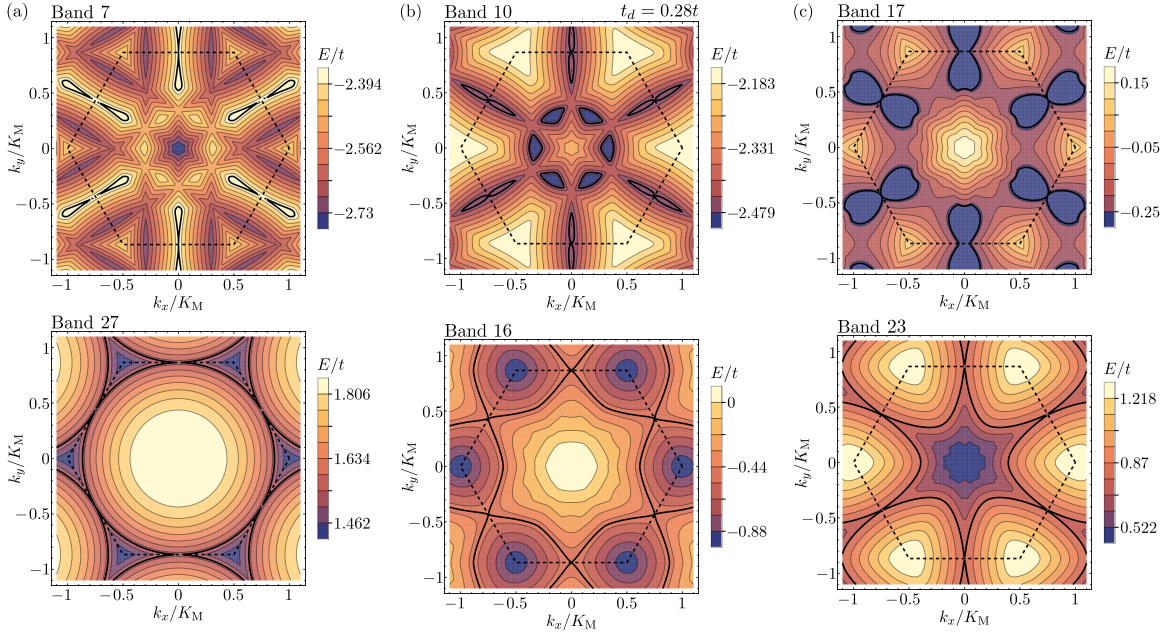
FIG. 14. Examples of second-order singularities appearing at the M_M point for AA (a), interlocked (b), and AB (c) stacked bilayers. Only for band 10 of interlocked TBK is a non-zero dimerisation used. The bold black lines denote the energy contour of the critical point, whilst the dashed line indicates the MBZ boundary. We take $\theta_c = 38.2°$, $a = 0.5338$ nm, $d_\perp = 0.6596$ nm, $t_H = 0$, $\phi = 0$, $t_\perp = 0.3t$, $\gamma = 20$ [28, 49] for the system considered here.

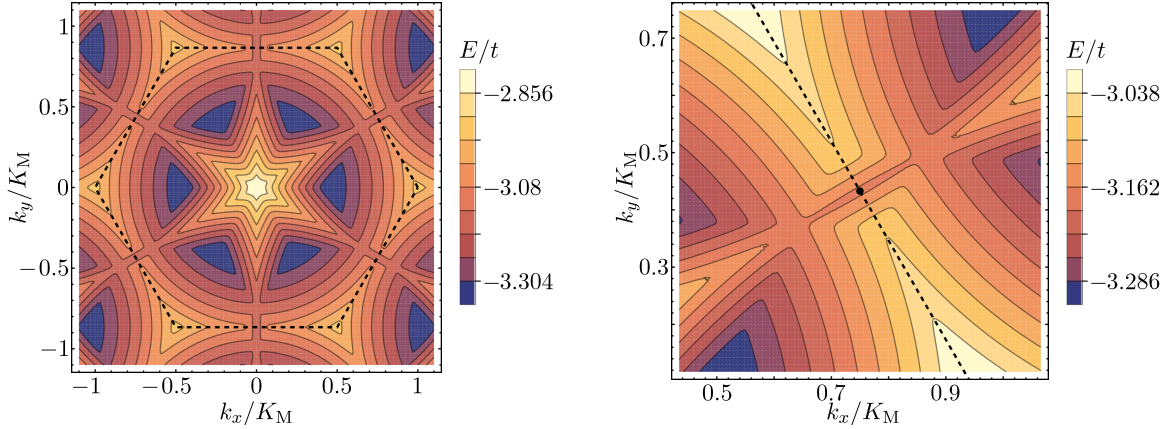FIG. 15. Potential fourth-order HOVHS about the M_M point in band 4 of AA TBK with no dimerisation. Similar features appear in band 4 of both interlocked and AB as well. We take $\theta_c = 38.2°$, $a = 0.5338$ nm, $d_\perp = 0.6596$ nm, $t_H = 0$, $\phi = 0$, $t_\perp = 0.3t$, $\gamma = 20$ [28, 49].

XIV. TOPOLOGICAL MONKEY SADDLES

In the main text, we presented an example of a topological monkey saddle for AA TBK with $\theta = 38.2°$. To show how the choice of stacking order greatly influences the topology of TBK, we consider the interlocked system with a Haldane tunneling for the same twist angle and tuned to yield a monkey saddle in the same band (band 20), with the band structure shown in Fig. 16a and energy contours of band 20 shown in Fig. 16c. The Chern numbers for each of these bands can be seen to change significantly from the AA scenario in Fig. 16b. In particular, whilst the type of HOVHS in band 20 remains unaffected by change in stacking order – a delocalised monkey saddle – its Chern number increases considerably from $\mathcal{C} = 3$ for AA stacking to $\mathcal{C} = 9$ for interlocked stacking. This suggests that the interplay of topology and interactions may be greatly enhanced in TBK when compared to other systems that typically host Chern numbers of order unity.
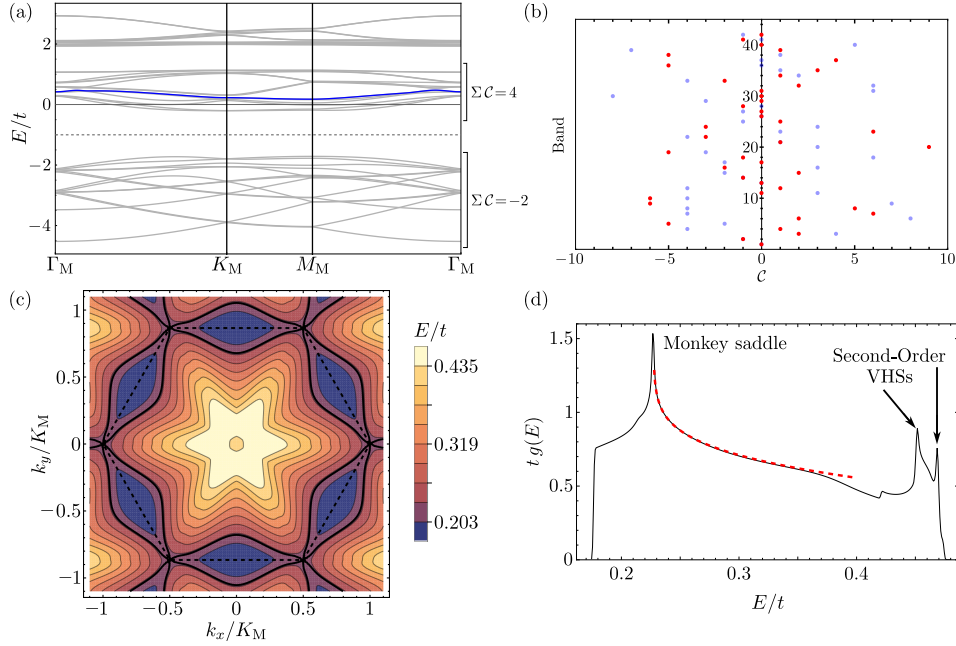
FIG. 16. Here we consider an interlocked TBK system with $\theta_c = 38.2°$, $a = 0.5338$ nm, $d_\perp = 0.6596$ nm, $t_H = 0.26589t$, $\phi = \pi/2$, $t_\perp = 0.3t$, and $\gamma = 20$ [28, 49]. (a): Band structure for the TBK system with band 20 highlighted in blue. (b): Chern numbers for interlocked TBK with band 20 tuned to a monkey saddle (red) and AA TBK with band 20 tuned to host a monkey saddle (faded blue). (c): Energy contours of band 20 with delocalised monkey saddles appearing at the MBZ corners. (d): Single-spin DOS per unit volume for band 20.
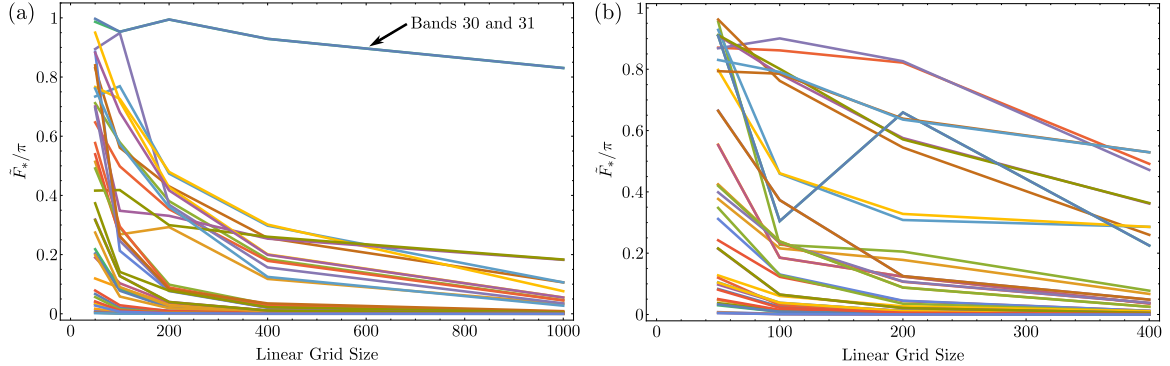

FIG. 17. Variation of the maximum absolute value of the lattice field strength for the 42 bands of the AA (a) and interlocked (b) TBK systems as the grid size is varied. Here we consider $\theta = 38.2°$, $a = 0.5338$ nm, $d_\perp = 0.6596$ nm, $\phi = \pi/2$, $t_\perp = 0.3t$, and $\gamma = 20$ [28, 49] with $t_H = 0.18147t$ (a) and $t_H = 0.26589t$ (b). Bands 30 and 31 are annotated specifically as they are what require larger grid sizes to obtain accurate calculation of the Chern numbers.

XV. NUMERICAL CALCULATION OF CHERN NUMBERS

In calculating the Chern numbers for the 42 bands presented in Fig. 4 of the main text, we found that discretising the MBZ into a 200×200 grid to be sufficient to obtain accurate results when using the method of Fukui et al. [71]. We confirmed this by performing the same calculation using both a 400×400 grid and 1000×1000 grid. We found it necessary to consider such large grid sizes due to bands 30 and 31 having an extremely small avoided crossing $\sim 10^{-6}t$. This resulted in a lattice field strength with a maximum magnitude of $\tilde{F}_* \sim 0.99\pi$ for bands 30 and 31 when using smaller grid sizes, indicating the possible loss of information in the plaquettes associated to this field strength when calculating the Chern number numerically. We show the variation of $\tilde{F}_*$ for all 42 bands as the grid size is changed in Fig. 17a. Here, we see its value for bands 30 and 31 reduces from the 200×200 grid onwards, reaching a value of $\tilde{F}_* \sim 0.83\pi$ for the 1000×1000 grid. The Chern numbers for all 42 bands did not change between the 200×200,

400×400, and 1000×1000 grids, indicating that the Chern numbers acquired from the 200×200 had converged. Moreover, the sum of the Chern numbers vanished for the 200×200 grid and above, whilst their sum failed to vanish for the 100×100 and 50×50 grids also considered in Fig. 17a. For comparison, when calculating the Chern numbers for interlocked TBK in Fig. 17b, we found that a 100×100 grid was sufficient to capture the topological nature of the bands, as shown by the variation of $\tilde{F}_*$ with grid size in Fig. 17b. We attribute this to the use of a larger complex tunneling energy, resulting in larger gaps between the bands and avoided high concentrations of Berry curvature.